THE JOURNAL OF
PHYSICAL
CHEMISTRY C
A JOURNAL OF THE AMERICAN CHEMICAL SOCIETY

pubs.acs.org/JPCC Article

Hydration Accelerates Radiative and Nonradiative Recombination in Small TiO_2 Nanoclusters

Published as part of The Journal of Physical Chemistry C special issue "Alec Wodtke Festschrift."

Miguel Recio-Poo, Mohammad Shakiba, Francesc Illas, Stefan T. Bromley,* Alexey V. Akimov,* and Ángel Morales-García*

Cite This: *J. Phys. Chem. C* 2025, 129, 1806−1823

Read Online

ABSTRACT: We report a nonadiabatic molecular dynamics (NA-MD) study on radiative and nonradiative recombination dynamics in small bare and hydrated titania nanoclusters, $(TiO_2)_4(H_2O)_m$ (m = 0, 2, 4) and $(TiO_2)_8(H_2O)_m$ (m = 0, 2, 5). Our findings indicate that increased hydration raises excitation energies and nonadiabatic couplings, accelerating both radiative and nonradiative recombination. We test the robustness of this predicted trend with respect to several important choices in our NA-MD methodology. We find that nuclear trajectories from classical force fields closely match those from density functional theory (DFT) calculations, with recombination time scales weakly dependent on the choice of pure or hybrid functionals. Additionally, decoherence corrections yield longer nonradiative recombination times than the overcoherent fewest switches algorithm. Overall, our predicted hydration-induced recombination acceleration in titania nanoclusters is found to be independent of the main choices in our NA-MD approach, thus giving us confidence in our results.

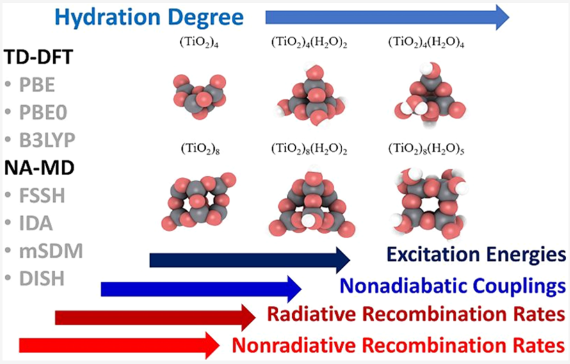

1. INTRODUCTION

As the global demand for energy continues to grow, the need for more efficient, environmentally friendly, and sustainable energy sources has become increasingly urgent. The ongoing development of heterogeneously photocatalyzed processes for solar energy conversion and sustainable energy production promises significant advancements in the quest for renewable energy solutions.[1,2] Heterogeneous photocatalysis involves the absorption of electromagnetic radiation by a solid catalyst to drive chemical reactions. This can be described as a physical phenomenon where an electron−hole pair is generated upon exposing a semiconducting material to light.[3−6] Light-harvesting constitutes the first step in heterogeneous photocatalysis and determines the capacity of a photocatalytic system to absorb incident photons and generate sufficient electron−hole pairs for the subsequent catalytic reactions.[7,8]

Among the wide variety of photoactive semiconductor materials, titanium dioxide (TiO_2), usually referred to as titania, stands out for its versatility in various photovoltaic and photocatalytic applications.[9−13] Many photoactive composite materials and heterostructures contain TiO_2 as a common ingredient, often functionalized with a metalorganic dye or quantum dots.[14,15] The onset for light absorption ranges from ~3.0 eV for the rutile polymorph to 3.2 eV for the anatase one. Hence, the minimum energy required to generate electron−hole pairs lies in the ultraviolet (UV) region. This large energy coupled with the high recombination rate of electron−hole pairs are the two important drawbacks causing low photoefficiency. To successfully overcome these limitations, several strategies have been explored. These involve dye- and quantum-dot-sensitization approaches,[16−18] nonmetal doping,[19−21] formation of nanostructured metal/semiconductor heterostructures,[22] or crystal facet engineering.[23−25] The ground state electronic structure derived properties of photoactive titania nanostructures can be tuned by tailoring the size, shape, composition, and degree of hydration,[26−32] making heterogeneous photocatalysis more efficient.

Understanding the dynamics of photoinduced processes is of fundamental interest for engineering titania-derived materials for practical photovoltaic or photocatalytic applications.[33] Indeed, several experimental and computational studies have been carried out to date to explore the nature and dynamics of excitons[34] and charge-carriers[35] in systems such as poly-

Received: October 22, 2024
Revised: December 31, 2024
Accepted: January 2, 2025
Published: January 10, 2025

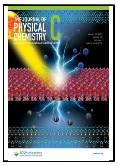

https://doi.org/10.1021/acs.jpcc.4c07180
J. Phys. Chem. C 2025, 129, 1806−1823

oxotitanates and anatase TiO_2 nanostructures using X-ray free electron lasers and pump−probe spectroscopy techniques.[36,37] Studies based on density functional theory (DFT) have been extensively employed to estimate the properties of excited electronic states in TiO_2 nanoparticles[38−42] and related systems.[43−45] Many of these studies rely on the single-particle (SP) description of electronic excited states and therefore may overlook multiconfigurational effects present in realistic excited states of such systems. Accounting for excitonic or multi-configurational many-body (MB) effects via a more rigorous linear-response (LR) time-dependent DFT (TD-DFT) framework was shown to lead to stronger nonadiabatic couplings (NACs) between electronic states and thus to faster excited states dynamics in many other systems compared to single-particle-based simulations.[46−48] However, simply employing the conceptually solid framework of LR-TD-DFT does not guarantee a quantitative description of the excitonic effects,[49,50] as the choice of the underlying density functional strongly affects the outcomes of such calculations. As such, the choice of a suitable exchange−correlation functional remains an open question.[51] For instance, widely used generalized gradient approximation (GGA) density functionals such as Perdew−Burke−Ernzerhoff (PBE)[52] are not capable of capturing the excitonic effects and may yield negative energies of the charge-transfer excitation within the TD-DFT framework.[53] On the other hand, the use of hybrid density functionals, especially range-separated, or even better−optimally tuned range-separated− is a common solution to overcome the limitations of GGA functionals.[54] However, the computational time scaling of DFT-based calculations is more expensive with hybrid functionals than with GGA functionals, especially at the TD-DFT level, making such calculations practically prohibitive for large systems. To the best of our knowledge, no excited state dynamics simulations based on TD-DFT description of electronic excitations, especially using hybrid density functionals, have been carried out for titania clusters so far.

Relying on the computed TD-DFT excitation energies and NACs connecting the states involved in the excitation, Non-Adiabatic Molecular Dynamics (NA-MD) is *de facto* trusted as the most comprehensive computational technique to investigate the excited state dynamics.[55−59] Recently, the electron injection,[60] photoexcited polaron dynamics,[61] and the effect of size/shape in bare TiO_2 nanostructures have been investigated through the NA-MD simulations.[41,42] However, as already mentioned, those approaches describe the excitations within a SP framework. In this way, while static TD-DFT calculations in TiO_2-related systems have been reported, they have not been utilized in the NA-MD calculations yet. As a result, a more reliable description of electronic dynamics in such systems is yet to be obtained.

Apart from the previous work of Muuronen et al.[62] who examined the mechanism of water oxidation on the surface of a $(TiO_2)_4$ cluster, we are not aware of other studies of the influence of chemisorbed water on excited-state dynamics in hydrated TiO_2 nanostructures. Considering that in realistic photocatalytic systems, the surfaces of photocatalytic TiO_2-based materials are most often covered with water, understanding the impact of water on the photoinduced dynamics of excited states of hydrated titania nanostructures is essential for providing a better understanding of the photocatalytic performance of these systems.

Here, we present a computational benchmark study of radiative and nonradiative dynamics in small bare and hydrated titania nanoclusters $(TiO_2)_4$ and $(TiO_2)_8$ conducted within a TD-DFT framework with hybrid density functional kernels. These system sizes have been previously studied and have been shown to be good models for capturing essential excited state dynamics in titania and similar systems,[37,63−65] providing a well-established framework for comparison and analysis. By computing the excited states dynamics in a systematically controlled series of systems, we explore the role of nanocluster size and the degree of hydration on the kinetics of the lowest excited state relaxation. Contrary to previously reported works, we utilize a MB description of the electronic excited states in these systems by using LR-TD-DFT with hybrid density functionals. We also conduct a systematic assessment of various components of our computational methodology. In particular, we investigate the applicability of the classical force fields to NA-MD calculations as a computationally feasible alternative to ab initio molecular dynamics (AIMD). We explore the role of hybrid density functional in such simulations. Finally, we conduct a comparative analysis of several trajectory surface hopping (TSH) and decoherence correction methodologies as applied to modeling nonradiative recombination in this class of systems. Overall, this work provides new detailed insights into the role of water in TiO_2 recombination dynamics while offering a detailed methodological evaluation for simulating nonadiabatic molecular dynamics.

2. MODELS AND METHODS

The investigation of the dynamic excited state properties is performed in photoactive titania nanoclusters including anhydrous and hydrated systems with the general chemical formula: $(TiO_2)_n(H_2O)_m$, for $n = 4$ (with $m = 0$, 2, and 4) and $n = 8$ (with $m = 0$, 2, and 5) (see Figure 1). The corresponding nanocluster structures used in all cases correspond to stable low energy minima found from global optimization searches.[66] These globally optimized nanoclusters are known to correspond well to the experimentally prepared hydrated TiO_2 species in cluster beams.[67] Based on the titania/water (m/n) ratio, our selection covers 0% as for the anhydrous $(TiO_2)_4$ and $(TiO_2)_8$ clusters, ~25% for $(TiO_2)_8(H_2O)_2$,

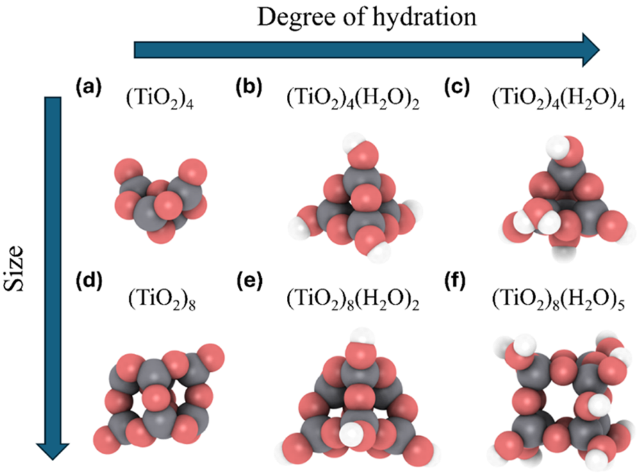

Figure 1. Anhydrous $(TiO_2)_4$ and $(TiO_2)_8$ (a, d) and hydrated $(TiO_2)_4(H_2O)_2$, $(TiO_2)_4(H_2O)_4$, $(TiO_2)_8(H_2O)_2$, and $(TiO_2)_8(H_2O)_5$ nanoclusters (b, c, e, f). Atom key: O—red, Ti—gray, H—white.

~50% for $(TiO_2)_4(H_2O)_2$, ~60% for $(TiO_2)_8(H_2O)_5$, and ~100% for $(TiO_2)_4(H_2O)_4$ hydration degrees. The larger $(TiO_2)_8$-based nanoclusters are most favorably hydrated by dissociated chemisorbed water molecules. In this way, terminal hydrogen (−H) and hydroxyl (−OH) groups bind with uncoordinated O and Ti atoms on the surface of the titania nanoclusters, respectively.[27] This dissociative hydroxylation mechanism is also favorable at initial hydration levels for the $(TiO_2)_4$ system. However, at ~100% hydration $(TiO_2)_4(H_2O)_4$, molecular adsorption occurs instead (as depicted in Figure 1c). The excited state photoreactivity of small titania nanoclusters with water has been studied experimentally[68] and computationally[69] but larger titania nanoparticles are typically considered in experimental photocatalysis studies. Here, our study of smaller nanoclusters aims to establish a reasonable benchmark for applying TD-DFT and NA-MD methodologies to larger photoactive nanostructures using hybrid functionals combined with the LR-TD-DFT calculations. More broadly, it provides an analysis of the role of nanocluster size and hydration degree in determining the resulting dynamic of lowest excited electronic states.

We focus on determining the electron−hole recombination dynamics using TD-DFT calculations to compute the ground state (S_0) population recovery kinetics starting from the first excited singlet state (S_1). The S_1 state represents an important stage in the relaxation process, as it is typically well separated from S_0 by a significant energy gap. The $S_1 \rightarrow S_0$ transition becomes the bottleneck of the excited state relaxation process and largely determines the overall efficiencies of photovoltaic materials.[70]

Our NA-MD simulation workflow involves four sequential steps. At each one of these steps, several methodological choices are possible which are systematically investigated as detailed below. The computational workflow is implemented as part of the open-source Libra package (v5.7.1),[71−73] which is used interfaced with the CP2K code (2023.1 version)[74] for computing all the quantities of interest.

Starting with the first step, two procedures are considered to generate the nuclear trajectories for all considered titania systems (see Figure 1). Such trajectories are next used to conduct the NA-MD calculations in the last step, as explained later. In the Born−Oppenheimer approximation, nuclear motion parametrically perturbs the electronic states and drives the evolution of the corresponding state amplitudes, so the nuclear trajectories obtained in this step for the electronic ground state are referred to as the guiding trajectories. Trajectories are generated via (i) classical MD simulations -using the NanoTiO,[75] and FFTiOH[66] interatomic potentials or force fields (FF) for respectively anhydrous and hydrated systems-, using the GULP4.4 package;[76,77] and (ii) AIMD using the CP2K package. In the latter case, the interatomic interactions are described at the DFT level using the semilocal PBE exchange−correlation functional.[52] The Kohn−Sham (KS) orbitals of valence electrons are expanded in an atom-centered double-ζ-valence-polarized (DZVP) basis set.[78] An auxiliary plane-wave basis is used to fit the electron density with an energy cutoff of 300 Ry. The core electrons for Ti and O are described using Goedecker-Teter-Hutter pseudopotentials.[79] Grimme's D3 method with zero damping is used to account for dispersion.[80]

As the choice of density functional may significantly impact the quality of molecular dynamics trajectories, its selection requires further justification. In this work, the PBE+D3 functional is chosen for its demonstrated accuracy in describing lattice parameters, energetics, and structural stability of various oxide systems.[81] The inclusion of dispersion corrections improves the quality of the standard PBE functional by effectively capturing van der Waals interactions, hence providing more reliable prediction for bulk and interfacial systems. Prior studies demonstrated that PBE and its variants perform well in modeling reaction pathways, diffusion, and interfacial dynamics.[82,83] Additionally, Ohto et al.[84] highlighted the suitability of dispersion-corrected GGA functionals like revPBE-D3(0) for water-based interfacial systems, balancing accuracy and computational cost.

Both FF-based MD and DFT-based AIMD simulations are conducted in the NVT ensemble with the target temperature of 300 K, generating a 4 ps trajectory. The temperature is maintained using the Nosé-Hoover thermostat[85] with the collision frequency parameter set to 100 fs^{-1}. A nuclear integration time step of 1 fs is used, giving rise to a trajectory composed of 4000 structures. The first 1000 fs are considered as an equilibration period, and our NA-MD calculations only use the data for the remaining 3000 nuclear configurations. The comparison of the NA-MD outcomes obtained using FF- and DFT-generated AIMD guiding trajectories allows us to better understand the influence of the level of theory on the resulting excited state dynamics. The atomic vibrational frequencies of our titania clusters along the 3000 fs runs provides a means to compare the two approaches. These vibrational frequencies can be obtained from the atomic velocity-velocity autocorrelation function (VV-ACF).[86] The Fourier transform of the VV-ACF yields the power spectrum which reveals the characteristic frequencies of the active nuclear modes in the MD calculations.

Once the trajectory is generated, the second step comprises TD-DFT calculations for each of the 3000 geometries sampled during the guiding trajectories. The TD-DFT calculations yield the energies of excited states, configuration interaction (CI) amplitudes of the key excited Slater determinants involved in all excited states of interest, as well as the time-overlaps of the selected KS orbitals. Despite that we are only interested in the dynamics involving S_0 and S_1 states only, it is important to compute other excited states, so the dynamical basis, including the vector made of all electronic states involved in the dynamics, is large enough to properly describe possible crossings between S_1 and other higher energy states. To this end, our basis includes up to ten excited states obtained from the TD-DFT calculations. The resulting excited states $\{\Psi_I = \sum_{a \in virt, i \in occ} c_{i,a} \Phi_i^a,\}$, are composed by superposition of excited Slater determinants (SDs) $\{\Phi_i^a = \hat{a}_i \hat{a}_a^+ \Phi_0\}$, which in turn are composed of the KS molecular orbitals (MO), $\{\psi_i\}$. Here, $\hat{a}_i \hat{a}_a^+$ are the Fermionic annihilation and creation operators, and Φ_0 indicates the ground state SD: $\Phi_0 = \det|\psi_{i_1} \psi_{i_2} ... \psi_{i_N}|$. The TD-DFT calculations also provide the excitation energy, E_i, the corresponding transition dipole between excited and the ground states, $\mu_{i,0} = \langle \Psi_i | \hat{\mu} | \Psi_0 \rangle$, as well as the corresponding oscillator strength, $f_{i,0} = \frac{2m_e}{3\hbar^2}(E_i - E_0)|\mu_{i,0}|^2$.

Similar to the VV-ACF described above, the autocorrelation function of the energy gap fluctuations characterizes the coupling of the nuclear modes to a particular electronic transition of interest.[87] In this approach, the fluctuation of the energy gap between states Ψ_i and Ψ_j is first computed, $\delta E_{i,j} = E_{i,j}(t) - \langle E_{i,j} \rangle$, where $E_{i,j} = E_i - E_j$. The Fourier transform of the gap ACF, $C(\tau) = \langle \delta E_{i,j}(\tau) \delta E_{IJ}(0) \rangle$ yields the influence

https://doi.org/10.1021/acs.jpcc.4c07180
J. Phys. Chem. C 2025, 129, 1806−1823

spectrum, $I(\omega)$, which shows the vibrational modes that strongly couple to the transition between states Ψ_i and Ψ_j. In our case, only states S_0 and S_1 are considered. The variance of the energy gap, $\langle \delta E_{i,j}^2 \rangle^{1/2}$ yields the pure dephasing times between such states,[87] a parameter used in some of our decoherence-corrected TSH calculations (e.g., mSDM):

$$\tau_{IJ} = \sqrt{\frac{12\hbar^2}{5\langle \delta E_{IJ}^2 \rangle}} \quad (1)$$

Besides nonradiative recombination which releases energy as heat through phonons, electrons and holes can recombine radiatively, emitting light. The probability of spontaneous photon emission is quantified by the Einstein $A_1 \rightarrow 0$ coefficient, while its inverse gives the radiative lifetime of the excited state, τ_r, computed as[88]

$$\tau_{r,1\rightarrow 0} = A_{1\rightarrow 0}^{-1} = \frac{3\pi\varepsilon_0\hbar c^3}{\omega_{10}{}^3\mu_{1,0}^2} \quad (2)$$

where $\omega_{10} = (E_1 - E_0)/\hbar$ is the transition angular frequency that determines the position of the spectral line in the absorption spectra. Again, $\mu_{1,0}$ represents the transition dipole moment between S_1 and S_0.

KS orbital time-overlaps described as $s_{ij}(t,t + \Delta t) = \langle \psi_i(t) | \psi_j(t + \Delta t) \rangle$, are also computed analytically as detailed elsewhere.[59] Since not all of the KS orbitals are involved in the excitations for the set of excited states of our interest, we only compute the time-overlap matrices for a subset of KS orbitals, which defines the orbital active space. The selection of such an active space is done globally, based on the analysis of the excitations for all nuclear geometries. The KS time-overlap matrices are used to compute the time-overlap matrices of Slater determinants using Lowdin approach,[89] $\langle \Phi_i(t) | \Phi_j(t + \Delta t) \rangle = \det | s_{a,b}(t,t + \Delta t) |_{a\in i,b\in j}$ where $a \in i$ represents that the KS spin−orbital a is present in the SD i and $| s_{a,b}(t,t + \Delta t) |_{a\in i,b\in j}$ represents a matrix of time-overlaps in the KS spin−orbital space.

The third step of the workflow computes the time-overlaps of the excited states included in the dynamical basis as a linear transformation of the SD time-overlap matrices by the CI coefficient matrices, $\langle \Psi_i(t) | \Psi_j(t + \Delta t) \rangle = \sum_{a,b} C_{a,i}(t) C_{b,j}(t + \Delta t) \langle \Phi_a(t) | \Phi_b(t + \Delta t) \rangle$. The resulting TD-DFT time-overlaps can be used to compute NACs, using the Hammes-Schiffer-Tully formula:[90]

$$d_{i,j}\left(t + \frac{\Delta t}{2}\right) \approx \frac{\langle \Psi_i(t) | \Psi_j(t + \Delta t) \rangle - \langle \Psi_i(t + \Delta t) | \Psi_j(t) \rangle}{2\Delta t} \quad (3)$$

As mentioned earlier, one of the aims of this work is to assess the role of the density functional choice in modeling radiative and nonradiative dynamics in titania systems. We consider PBE,[52] a semilocal GGA functional, as well as PBE0[91] and B3LYP,[92] which are hybrid functionals incorporating 25% and 20% of the exact Fock exchange, respectively. The use of hybrid functionals mitigates the underestimation of the charge-transfer energy typically present for calculations with the PBE functional. In addition, prior studies reported that NACs may be overestimated when pure functionals such as PBE are used, especially at the single-particle level.[93]

Finally, NA-MD calculations are performed in the last step of the workflow to predict the coupled evolution of the nuclei and electrons. The starting point of this calculation represents the time-evolved overall wave function of the system in a basis of the adiabatic excited states (dynamical basis), $\{\Psi_i(\boldsymbol{R}(t))\}$, implicitly dependent on time via nuclear geometries:

$$\tilde{\Psi}(t) = \sum_i C_i(t) \Psi_i(\boldsymbol{R}(t)) \quad (4)$$

The amplitudes, $C_i(t)$, evolve according to the time-dependent Schrodinger equation (TD-SE):

$$i\hbar C_i(t) = \sum_j H_{i,j}^{vib}(\boldsymbol{R}(t)) C_j(t) \quad (5)$$

where the matrix elements of the vibronic Hamiltonian, H_{ij}^{vib}, are given by

$$H_{ij}^{vib}(\boldsymbol{R}(t)) = E_i(\boldsymbol{R}(t))\delta_{ij} - i\hbar d_{ij}(\boldsymbol{R}(t)) \quad (6)$$

Here, E_i are the state energies, δ_{ij} is the Kronecker delta, and d_{ij} are the NACs introduced in eq 3. The TD-SE in eq 6 is solved using the local diabatization (LD) approach,[94,95] which is known to be more robust compared to the NAC-based integration method. The neglect-of-back-reaction approximation (NBRA)[96−98] is used according to which the electronic dynamics is affected by the nuclear dynamics, but the latter is not responsive to change of the electronic state.

The time-evolved TD-SE amplitudes are used in the TSH algorithms to stochastically sample electronic transitions. Here, four TSH algorithms are used (i) the Tully's fewest switches surface hopping (FSSH),[99] (ii) revised decoherence-induced surface hopping (DISH_rev2023),[100,101] (iii) instantaneous decoherence at attempted hops (IDA),[102] and (iv) the modified simplified decay of mixing (mSDM).[100] While the FSSH algorithm is known for its overcoherent nature, the other three approaches introduce electronic decoherence in different ways and thus are assumed to be more reliable.

The NA-MD calculations are carried out for 3 ps with both electronic and nuclear integration time steps taken as 1 fs. In fact, the nuclear time steps are already predetermined by the MD trajectories obtained in the first step of the overall workflow. The use of the LD integration allows the electronic timesteps to be as large as the nuclear ones. The NA-MD calculations are averaged over 30 initial nuclear conditions that are taken as points of the guiding trajectories and separated by 100 fs. All NA-MD calculations are initiated in the first excited state. For each initial condition (starting geometry and electronic state), 500 stochastic realizations of the TSH process are computed. The averaging over the stochastic realizations yields the results for each batch. The averaging over all batching is used for obtaining a more statistically accurate description of the dynamics as well as to obtain the estimates of the margins of errors for the computed relaxation time scales.

To compute the nonradiative recombination times, we track the population of the ground state, which is fitted by the stretched-exponential function:

$$f(t) = 1 - \exp\left(-\frac{t}{\tau}\right)^{\beta} \quad (7)$$

where, τ and β are fitting parameters, with the former having the interpretation of the lifetime. The β parameter is allowed to vary between 1 and 2 to account for two limiting cases − the Gaussian kinetic ($\beta = 2$) typical for overcoherent methods, and the exponential kinetics ($\beta = 1$) characteristic for the decoherence-corrected calculations. The computed error bar

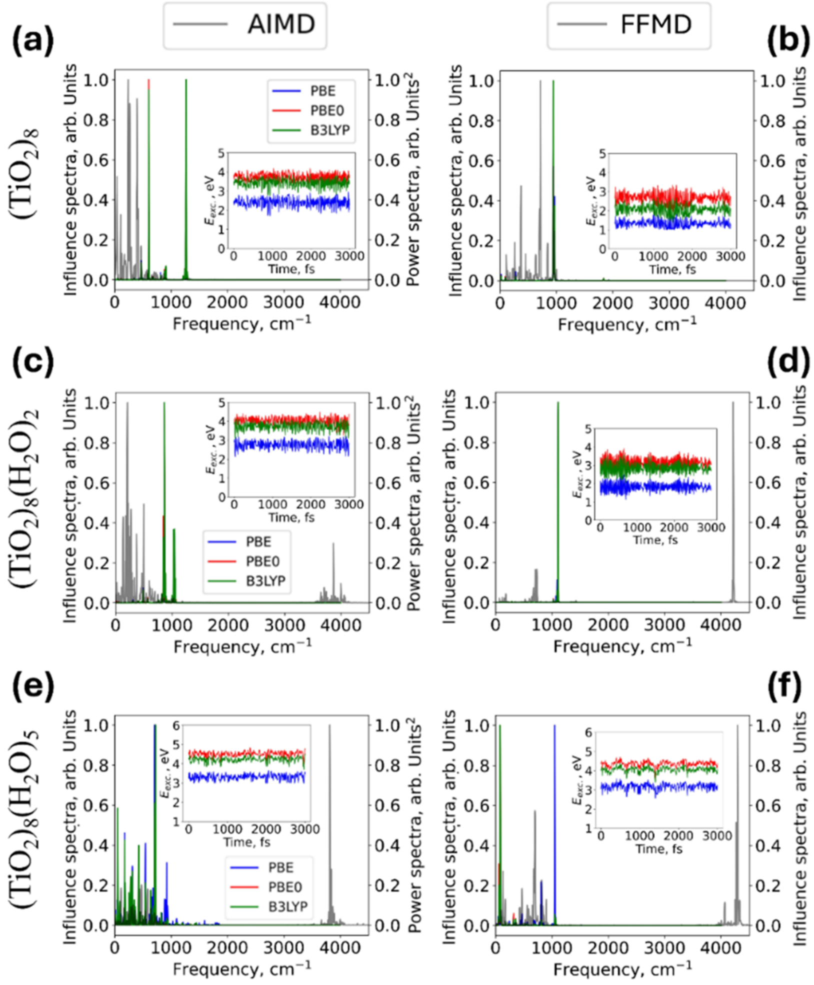

Figure 2. Normalized power (gray) and influence (red) spectra for $(TiO_2)_8$ (a, b), $(TiO_2)_8(H_2O)_2$ (c, d) and $(TiO_2)_8(H_2O)_5$ (e, f) systems. The power spectra are computed using nuclear trajectories obtained with AIMD (a, c, e) or classical FFMD (b, d, f) methods. The influence spectra characterize the vibrational modes that drive the transition between the ground state and first excited state. The insets show the evolution of the ground-to-first-excited-state energy gap in corresponding calculations. Color codes: gray−power spectra, blue, red and green−influence spectra. For the influence spectra, TD-DFT-calculated excitation energies are computed with B3LYP (green lines), PBE0 (red lines) and PBE (blue lines) functionals.

for each trajectory with respect to the average population evolution branch is computed as

$$\epsilon = Z\frac{s}{\sqrt{N}} \tag{8}$$

where s is the standard deviation of the τ parameters sampled from $N = 30$ batches. Following the prior practice,[103] we select the samples having a R^2 value of more than 0.1. Lastly, the Z value is the confidence interval coefficient. For a confidence interval of 95%, it is equal to 1.96.

3. RESULTS AND DISCUSSION

In this section, we present the results in a manner congruent with the above-discussed steps of our NA-MD protocol, i.e., the generation of nuclear trajectories, excited states computation, NACs calculation and excited state dynamics analyses. We perform a comparative analysis of the computational approaches at different steps of the workflow. We discuss the effect of the choice of the method used to obtain the vibrations activated during the generated guiding trajectories, the role of the density functional choice in determining the excited state energies and NAC derived from the TD-DFT calculations. We show a qualitative comparison of the dynamics generated by different TSH schemes within the NA-MD calculations. Further, we analyze chemical aspects of the systems, such as the role of the hydration degree and cluster size on the excited state relaxation times in the selected titania nanoclusters (see Figure 1).

3.1. Power and Influence Spectra. We start comparing the ground state MD trajectories obtained using either FFMD or AIMD by computing the power and influence spectra of the $(TiO_2)_8$, $(TiO_2)_8(H_2O)_2$, and $(TiO_2)_8(H_2O)_5$ systems (Figure 2). Analogous calculations for the $(TiO_2)_4$-derived clusters are reported in Figure S1 of the Supporting Information (SI). The power spectrum (gray lines) represents the vibrational modes that are activated/appeared in the MD trajectory. In the limit of sufficiently long ergodic evolution, this spectrum should also relate to the vibrational density of states with the difference that it also accounts for anharmonic effects, unlike the conventional normal modes analysis. The influence spectrum (colored lines in Figure 2 and Figure S1 of the SI) represents the modes that are coupled to the electronic transition between the states of interest (i.e., S_0 and S_1). To facilitate comparison and visualization, both the influence spectrum and power spectrum are normalized by dividing all values by their respective maximum values, such that the highest value is one. In addition to the choice of method used to generate nuclear trajectories (i.e., FFMD or AIMD), the influence spectra also depend on the electronic structure method used to compute the electronic states. The evolution of the first excited state energy derived from the TD-DFT calculations is shown in the insets of Figure 2. As outlined in the methodology section, the ACF of the excitation energy fluctuation is what determines the frequencies of the modes coupled to the $S_1 \rightarrow S_0$ transition.

Power spectra of the bare $(TiO_2)_8$ cluster (Figure 2a,b) show the vibrational modes at frequencies similar to those observed in titania bulk phase. The vibrational modes ranging between 100 to 200 cm^{-1} correspond to Ti−O stretching modes,[104] while those ones associated with Ti−O−Ti angle bending are in the 500−1000 cm^{-1} range.[105−107] The power spectra of all hydrated $(TiO_2)_8$ clusters (Figure 2c−f) show a characteristic hydroxyl stretching mode around 3700−3900 cm^{-1}.[27] For a fixed nuclear trajectory method, the position and the broadening of the OH-stretching modes are nearly insensitive to the degree of hydration. Qualitatively, the vibrational modes obtained from FFMD are similar to those originating from AIMD (PBE-MD). Although the exact positions of the peaks differ from each other in the two approaches, the power spectra are qualitatively the same. Compared to the AIMD results, the FFMD ones tend to yield slightly blue-shifted overall spectra with a smaller number of well-pronounced peaks. The reduced number of peaks in the FFMD calculations is likely due to the more simplified description of interatomic interactions described by NanoTiO and FFTiOH FFs with respect to the more accurate electronic description of bonding in DFT-based AIMD calculations. The systematically lower frequencies in the AIMD spectra with respect to the FF-based one may be attributed to a better description of anharmonic effects in the former approach. The anharmonicities also realize the cross-coupling of vibrational modes and vibrational energy redistribution between them. Thus, vibrational energy is more likely to diffuse between different modes and activate them, in addition to resonances of vibrational modes. As a result of these two effects, the AIMD approach generates denser vibrational densities of states compared to the FFMD dynamics. Despite the noted differences, the high degree of resemblance between spectra computed with FFMD or DFT-based AIMD points out that the tested FFs are sufficiently accurate to act as computationally efficient counterparts to DFT calculations in potential studies of larger titania-derived systems,[108] where the AIMD based approaches become unattainable.

Figure 2 also shows the influence spectra and the energy evolution of the first excited state (insets) computed for $(TiO_2)_8$-based clusters using TD-DFT calculations with three density functionals: PBE (blue), PBE0 (red) and B3LYP (green). Figure S1 of the SI shows analogous information for $(TiO_2)_4$-based clusters. All spectra indicate that the $S_1 \rightarrow S_0$ transition is driven by the Ti−O−Ti angle bending modes that are in the 500−1000 cm^{-1} range. This finding is in agreement with the previous studies of Alvertis et al.[109−111] who discussed the dominance of low-frequency vibrations in shaping exciton dynamics and influencing nonradiative processes.

In particular, the mode at around 1000 cm^{-1} is present for all methods and in all systems (see Figure 2). Notably, the mode appears to be split when DFT is used for computing the guiding trajectory (e.g., the peaks in the 500 to 1400 cm^{-1} range), while it consists of only one strong peak at around 1000 cm^{-1} when the FF is used for producing the guiding trajectory. The splitting observed in AIMD DFT-based spectra is likely due to the activation of different modes due to the anharmonic effects enabling the vibrational energy transfer between the modes and hence their appearance in the spectrum. This effect is rather general since the AIMD influence spectra show a larger number of modes coupled to the electronic transition of interest than the FF-based influence spectra. The Ti−O stretching modes in the 100 to 200 cm^{-1} range do not show strong coupling to the electronic transition of interest in neither bare nor weakly hydrated clusters (Figure 2a−d). However, these modes are present in the strongly hydrated system and only when DFT is used for producing the guiding trajectory (Figure 2e).

Although all methods show the hydroxyl vibrational modes around 3000 cm^{-1} in the power spectra, this mode is not coupled to the $S_1 \rightarrow S_0$ transition as it is not present in the influence spectrum. Similar results and trends are obtained for the smaller $(TiO_2)_4$-based nanoclusters, as reported in Figure S1 of the SI, suggesting that both power and influence spectra features are size-independent. The strongly hydrated cluster (i.e., $(TiO_2)_4(H_2O)_4$) may need further analysis though, given the different cluster structures rendered by the use of either AIMD- or FF-based trajectories. While the initial shape of the globally optimized structure with an adsorbed water molecule (Figure 1c) is maintained throughout the whole AIMD runs, the use of FFs gives rise to a more symmetric structure which, is slightly higher in energy than the AIMD one. This is due to the intrinsically more simplified nature of the FF parametrized interatomic interactions. Figure S2 shows a comparison between both hydrated NPs at the end of each MD nuclear trajectory. The discrepancies in the morphologies between both NPs thus lead to different power and influence spectra features, especially at around 1500 cm^{-1} (Figure S1e) likely due to the isolated water molecule vibrational modes shifting back to their original frequencies.

3.2. TD-DFT Excited State Energies and NACs.

To rationalize the contributions from different vibrational modes as shown in the influence spectra, we analyze the electronic densities corresponding to the highest occupied molecular orbital (HOMO) and the lowest unoccupied molecular orbital (LUMO) of the $(TiO_2)_4(H_2O)_m$ (m = 0, 2, and 4), and $(TiO_2)_8(H_2O)_m$ (m = 0, 2, and 5) nanoclusters. For each system, we select a representative geometry sampled from the precomputed MD trajectory and visualize the orbital iso-value surfaces computed with the PBE density functional (see Figure 3). For all considered functionals, we find that the composition of the lowest excited TD-DFT state, S_1, is dominated by the HOMO → LUMO excitation, as can be quantified by the squares of the CI coefficients with which they mix in the TD-DFT “wavefunctions” (Table S1 in the SI). The PBE functional shows a large dominance of the HOMO → LUMO excitation (larger single-particle character), hence its use as a representative case in Figure 3. We thus only focus on the frontier orbitals to rationalize the observed features of the influence spectra. Regardless of the hydration degree, the larger electronic densities are located around the Ti−O bonds. Thus, the Ti−O bond stretching as well as O−Ti−O or Ti−O−Ti angle bending modes can affect the corresponding MOs and excited states the most and hence reveal themselves in the influence spectrum.

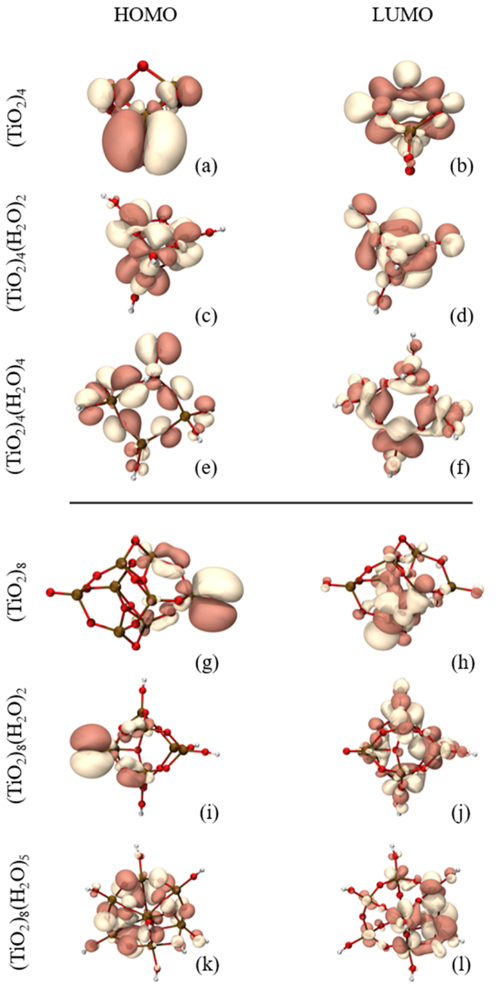

Figure 3. Isosurfaces of HOMO (a, c, e, g, i, and k) and LUMO (b, d, f, h, j, and l) orbitals corresponding to (a–f) $(TiO_2)_4$-based and (g–l) $(TiO_2)_8$-based sets of titania nanoclusters. The cluster geometries are sampled from the corresponding FF-based MD trajectories. Isosurface values are 0.012 $Å^{-1/3}$ (tan) and −0.012 $Å^{-1/3}$ (white). Multiwfn software[112] was employed to generate the isosurfaces. Atom key: O—red, Ti—brown, H—white.

The above argument does not always hold for TD-DFT calculations based on either PBE0 or B3LYP hybrid functionals. The TD-DFT pseudowave functions computed with such hybrid functionals exhibit larger mixing of other single-particle configurations (see Table S1 of the SI). Nevertheless, the orbitals involved in other mixed configurations are in almost all cases localized on the Ti−O fragments (Figure S3 of the SI), and not on the hydroxyl groups. This confirms that the influence spectra are systematically insensitive to the hydroxyl vibrational modes regardless of the exchange−correlation functional used.

The analysis of the trajectory-averaged first excited state energy computed with different methods reveals that the hydration of titania nanoclusters induces a systematic increase of the trajectory-averaged vertical excited state energies, $\overline{E_{exc}}$ (see Figure 4a,b in and insets in Figure 2). We rationalize this effect by two factors, (i) energy gap opening due to the removal of defect states (i.e., uncoordinated O and Ti sites), and (ii) weaker stabilization of charge transfer excitations in hydrated systems. First, the hydration of titania nanoclusters promotes the electronic energy gap opening, as estimated by the HOMO−LUMO difference by passivating defect midgap states originated due to under-coordinated (O_{1c} and Ti_{4c}) surface atoms in the bare or weakly hydrated $(TiO_2)_4$ systems. By increasing the hydration of titania nanoclusters, the "defect" states are removed more completely thus opening the energy gap. This mechanism was already reported by some of us in previous works.[28,66] Second, excited states exhibit more isotropic charge distributions in strongly hydrated systems, leading to smaller excited-state dipole moments and, consequently, reduced Coulombic stabilization of these states. This effect contributes to an increase in the excitation energy of the strongly hydrated clusters. Besides the two main factors detailed above, the cumulative effect of the dipolar −OH ligands introduces an additional electric fieldon the hydrated nanocluster core, which has been shown to influence the energy of frontier orbitals/band edges.[113−115] However, this effect is expected to be similar in both frontier levels and not be correlated with gap opening.

The charge distribution (ii) point raised can be explained by means of the analysis of the orbitals involved in the excitations. The analysis of the CI amplitudes suggests that the S_1 states of nearly all considered clusters are dominated by the HOMO → LUMO excitation. For the bare $(TiO_2)_8$ nanocluster, such a transition is a longer-distance charge transfer that creates a strong dipole moment (Figure 3g,h). The resulting charge-separated state has a notable Coulombic interaction between electron and hole which lowers the energy of the corresponding excited state to a larger extent than in the smaller $(TiO_2)_4$ nanocluster. With the increased degree of hydration, both HOMO and LUMO involved in the excitation tend to become more spatially isotropic and more delocalized. The corresponding HOMO → LUMO transition thus results in a shorter-distance charge transfer, leading to a smaller S_1 dipole moment and a smaller Coulombic stabilization and hence in higher excitation energy of the S_1 excited state. This rationalization is consistent with the magnitudes of the trajectory-averaged dipole moment of S_1 state for all systems compiled in Table S2 of the SI. It should be noted that although the magnitudes of the excited state dipole moment can be indicative of the amount of charge separation in the excited states, other factors such as exchange and correlation effects may come into play nontrivially.

In nanocluster systems, such as those considered in this work, the confinement of electronic states limits the extent of dipole coupling, which reduces the influence of the long-range Fröhlich mechanism that plays a dominant role in nonradiative recombination processes in extended systems (such as bulk TiO_2).[116] This mechanism arises from dipole interactions facilitated by the delocalized nature of electronic states in the bulk, leading to significant long-range effects. However, for small TiO_2 nanoclusters, the electronic and vibrational dynamics differ significantly due to spatial confinement. In this way, short-range coupling mechanisms, realized by localized vibrations and interactions within the cluster become more prominent. Furthermore, surface effects, particularly in hydrated nanoclusters, strongly impact the vibrational modes and charge dynamics, further amplifying the role of short-range coupling.

We observe that the $(TiO_2)_4$ nanocluster exhibits larger $\overline{E_{exc}}$ values than the $(TiO_2)_8$ counterpart for all considered methodologies. This effect can be initially attributed to quantum confinement becoming more prominent when decreasing the nanocluster size. However, the influence of

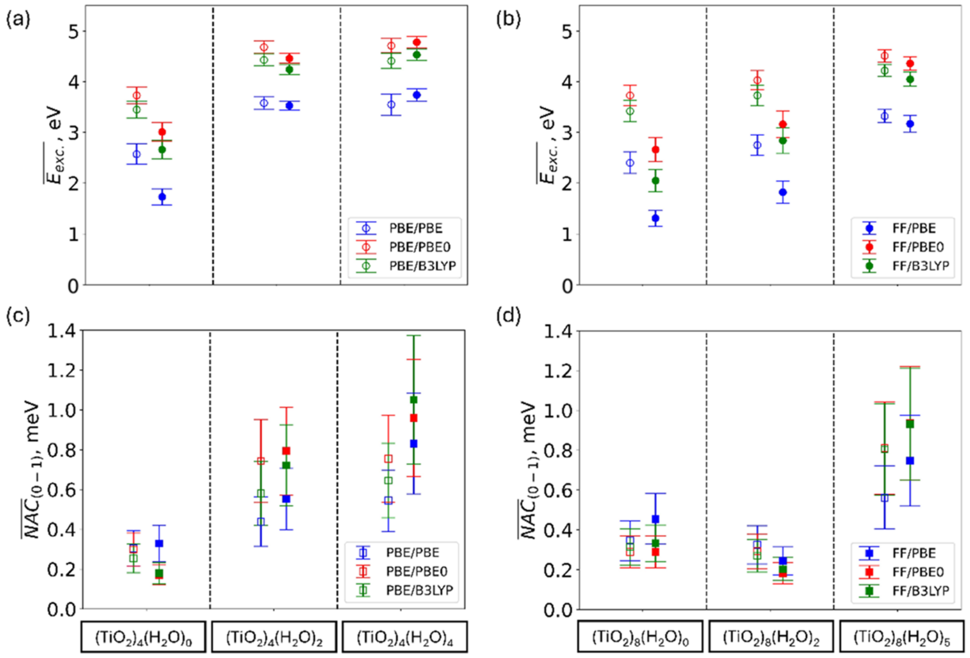

Figure 4. (a, b) Trajectory-averaged values of the first excited state energies (obtained with three DFT functionals) for each of the six clusters. Color codes: blue, red and green − PBE, PBE0, and B3LYP functionals. Empty and solid circles correspond respectively to DFT-based and FF-based nuclear trajectories. (c, d) Trajectory-averaged values of the trajectory-averaged nonadiabatic couplings between ground (S_0) and first excited state (S_1) obtained with three DFT functionals for each of the six clusters. Color codes: blue, red and green—PBE, PBE0, and B3LYP functionals. Empty and solid squares correspond respectively to DFT-based and FF-based nuclear trajectories. Error bars represent the standard deviation for each of the calculations.

quantum confinement at these small sizes can be overshadowed by the effects from specific atomic bonding or the presence of defects in the material. This effect is maintained for the hydrated nanoclusters, e.g., the saturated $(TiO_2)_4(H_2O)_4$ also displays larger $\overline{E_{exc}}$ values than the than the highly hydrated $(TiO_2)_8(H_2O)_5$ nanocluster (see Figure 4a,b and Table S3 of the SI).

There are two methodological issues to explore here: (i) the dependence of $\overline{E_{exc}}$ on the choice of density functional, and (ii) its dependence on the choice of method to produce the trajectories (FFMD *vs* AIMD). First, expectedly, PBE yields systematically the lowest $\overline{E_{exc}}$ values among all the functionals tested. This observation holds for all nanoclusters regardless of the methodology to obtain the trajectories. The shortcomings of pure density functionals such as PBE when used in TD-DFT calculations of excited states, especially those having charge transfer character, are well-known.[117,118] They originate from the incorrect (short-range) behavior of the exchange functional leading to overdelocalization of excited states and significant underestimation of energies of charge transfer states, sometimes including negative excitation energies,[53] and overestimation of NACs.[93] Since the problems are more apparent in extended systems, for the smallest bare $(TiO_2)_4$ nanocluster we observe surprisingly accurate excitation energy using the TD-DFT (PBE) method. Using the DFT-based AIMD nuclear trajectory, the TD-DFT calculation with the PBE functional estimates the $\overline{E_{exc}}$ value for S_1 state to be 2.57 eV, which is perhaps fortuitously closer to the one reported in experiments (2.60 eV)[119] than the ones provided by TD-DFT with PBE0 (3.73 eV) or B3LYP (3.45 eV) functionals. Repeating a similar analysis for the FF-based nuclear trajectory, the underestimation of the S_1 excited state energy by TD-DFT calculations with the PBE functional is more noticeable (1.73 eV). In this case, computing the excitations with the PBE0 (3.01 eV) and specially B3LYP (2.66 eV) functionals lead to values more in line with experiments.

Second, we observe that using FF-derived trajectories instead of the AIMD-based ones generally yields a reasonable agreement of computed $\overline{E_{exc}}$ values. This agreement is improved as the degree of hydration (i.e., m/n) ratio increases. For bare $(TiO_2)_n$ clusters, the largest discrepancies in $\overline{E_{exc}}$ are observed the FF-based nuclear trajectories, which are underestimated by more than 1 eV compared to the DFT-based one. For instance, the case of $(TiO_2)_8$ nanocluster with excitation energies of 1.31 eV (FFMD/PBE), 2.66 eV (FFMD/PBE0), and 2.05 eV (FFMD/B3LYP) vs 2.40 eV (AIMD/PBE), 3.73 eV (AIMD/PBE0), and 3.42 eV (AIMD/B3LYP), respectively. This decrease of the excitation energies can be tentatively attributed to the more symmetrical structures favored by the FF employed to obtain the trajectory. As the degree of hydration increases, the differences in $\overline{E_{exc}}$ tend to become smaller (e.g., 3.17 eV (FFMD/PBE), 4.36 eV (FFMD/PBE0), and 4.05 (FFMD/B3LYP) eV vs 3.32 eV (AIMD/PBE), 4.51 eV (AIMD/PBE0), and 4.22 eV (AIMD/B3LYP) in the case of $(TiO_2)_8(H_2O)_5$ case). The differences in $\overline{E_{exc}}$ values computed with AIMD- or FF-based trajectories become smaller with increased hydration. We note that the tendency of the currently employed FFs to yield more symmetric structures may be problematic in larger titania NPs, where the surface/volume fraction is small and where hydration does not induce a large degree of structural symmetry breaking. Such simulations would likely underestimate the excitation energies and hence overestimate the nonradiative recombination rates. This issue could be alleviated by employing more accurate FFs with more sophisticated parametrizations (e.g., reactive FFs) or machine learned FFs.

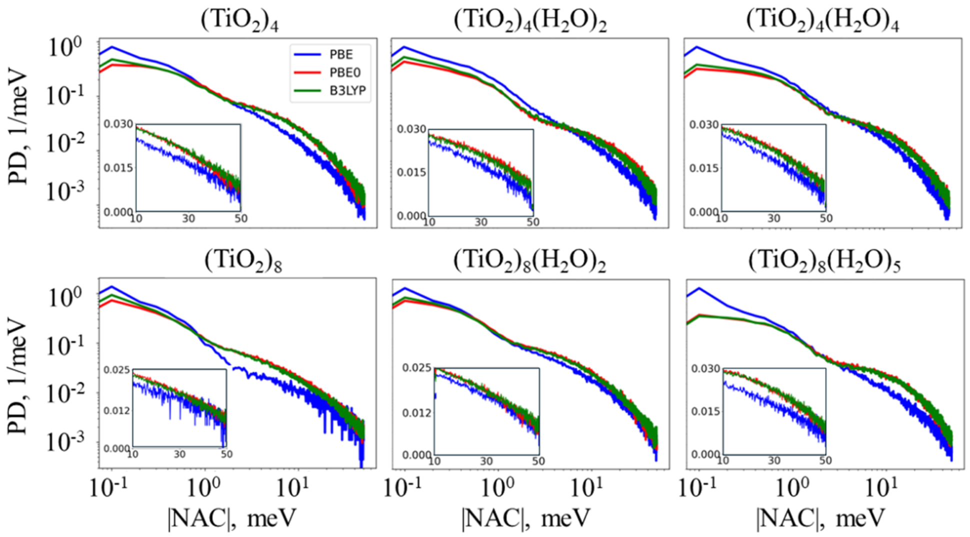

Figure 5. Computed probability distribution (PD) of NACs between pairs of all states in our dynamical basis for all clusters (AIMD-based nuclear trajectories). The inset graphs provide a zoom-in to the larger NACs values region, unveiling larger probability densities with hybrid functionals in most cases.

We now focus on the analysis of the trajectory-averaged nonadiabatic coupling ($\overline{\mathrm{NAC}}$) between S_0 and S_1 states as computed with the TD-DFT methodology (Figure 4c,d and Table S4 of the SI). With a few exceptions, the average NAC values obtained for FF-based trajectories are somewhat higher than those for the AIMD-based trajectories, although the values lie within each other's error margin, for each selected combination of system and density functional. Thus, the use of the FF-based trajectories appears to be a reasonable approach for computing NACs when computational demands do not allow using DFT-based AIMD trajectories.

The $\overline{\mathrm{NAC}}$ values gradually increase with the increase of the degree of hydration. This effect is, in principle, counterintuitive because the NAC between a pair of states should be inversely proportional to the energy gap between such states. However, the NACs can be regarded as a quantification of the wave function change upon a nuclear perturbation. Thus, for NACs to be large, it is important that (i) the vibrations that couple to the pair of states of interest are activated, and (ii) the wave function changes with symmetries that are distinct to the symmetries of the corresponding vibrational modes. As the degree of hydration increases, the electronic wave functions (specifically the HOMO and LUMO) involved in the $S_0 \rightarrow S_1$ transition tend to become more delocalized. This delocalization arises from the interaction between the nanocluster and surrounding water molecules, which induce polarizing effects and stabilize specific electronic states. The broader spatial extent of delocalized wave functions enhances their sensitivity to nuclear motions. Consequently, additional vibrational modes capable of efficiently coupling to the $S_0 \rightarrow S_1$ electronic transition can be activated, leading to larger average NACs. This is also apparent from the influence spectra in Figure 2 and Figure S1 of the SI. This explanation is also consistent with the presence of an apparent threshold of switching between NACs being sensitive or not sensitive to the degree of hydration of the titania nanoclusters. Indeed, in the small $(TiO_2)_4(H_2O)_m$ nanoclusters, the surface/volume ratio is larger than in the larger $(TiO_2)_8(H_2O)_m$ nanoclusters. Thus, the surface water molecules cause more significant disorder in the former systems leading to immediate nearly linear dependence of $\overline{\mathrm{NAC}}$ on the number of water molecules (Figure 4c). In the $(TiO_2)_8(H_2O)_m$ systems, we first observe a plateau suggesting no dependence of $\overline{\mathrm{NAC}}$ on the degree of hydration. As this number increases, the disorder caused by the surface hydration becomes sufficient to affect the wave functions and increase the $\overline{\mathrm{NAC}}$ values (Figure 4d). The current explanation of the influence of orbital localization on the electron−phonon (or, equivalently, NA) coupling is also in line with the analogous arguments discussed in multiple prior works, although focused on other systems.[55,59,110,120]

Although the above analysis focuses on comparing the averaged NAC values, it is important to note that it is the instantaneous NACs and their distribution what ultimately determines the dynamics of excited state relaxation. Following prior works,[59,103] we compute the distributions of NACs for all systems and using all considered density functionals (Figure 5). Despite the discussed differences in the average NACs between the first excited and the ground states, we observe relatively similar distributions for all systems. These plots are especially convenient for discussing the dependence of NACs on the chosen density functional. As seen from the peaks of the distributions (which gravitate to smaller NAC values), there is a smaller probability to sample smaller NACs when using hybrid functionals (PBE0 or B3LYP) compared to those computed with the PBE functional. These results are consistent with the previous work showing that the use of hybrid functionals leads to decreased NAC values in the KS basis compared to the pure-functional counterparts, especially in rather large systems.[93] Additionally, we observe that the large couplings are more probable when hybrid functionals are used instead of PBE. This effect can be rationalized by the fact that the present couplings are computed at the TD-DFT level rather than at the single-particle one. Indeed, the configurational mixing in TD-DFT wave functions facilitates larger couplings.[47,48] As we mentioned above, hybrid functionals also increase the configuration mixing in the TD-DFT states of $(TiO_2)_n(H_2O)_m$ systems, thus their use leads to higher likelihood of generating larger NACs.

3.3. Nonradiative Recombination.

The main outcomes of our NA-MD simulations are the nonradiative recombination

https://doi.org/10.1021/acs.jpcc.4c07180
J. Phys. Chem. C 2025, 129, 1806−1823

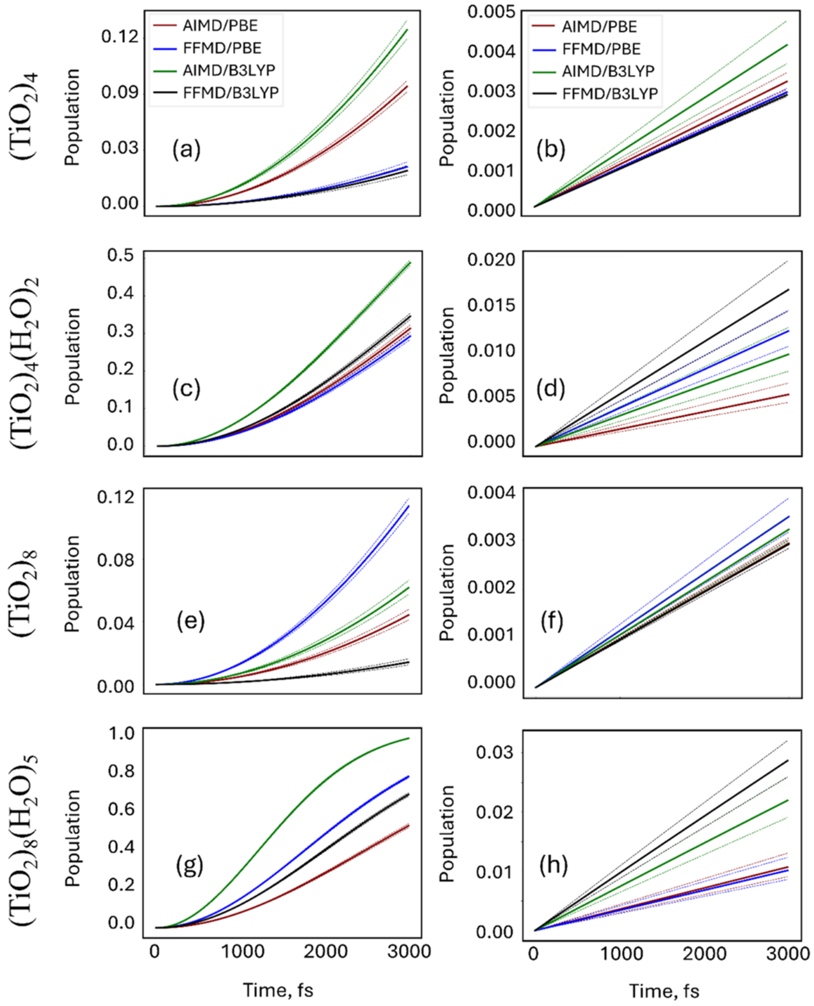

Figure 6. Ground state (S_0) population evolution with FSSH (a, c, e, and g panels) and mSDM (b, d, f, and h panels) TSH approaches. First and second rows (a−d) correspond, respectively, to $(TiO_2)_4$ and $(TiO_2)_4(H_2O)_2$ systems: third and four rows (e−h) to $(TiO_2)_8$ and $(TiO_2)_8(H_2O)_5$ nanostructures. Concerning the underlying DFT functional for computing the excitations, red and blue lines are associated in each plot to PBE, while green and black correspond to the hybrid B3LYP functional. On the other hand, red and green refer to PBE-based AIMD nuclear trajectories, while blue and black to trajectories obtained with FFs. The average population for each case is shown in bold lines, whereas dashed lines account for the error bars at each time.

rates from the first excited state S_1 to the ground state S_0 reported in Figures 6, 7, and Table 1. The $S_1 \rightarrow S_0$ transition corresponds to the charge carrier recombination process, so we often refer to the corresponding time scale as the recombination time. In particular, we focus our analysis on how these times vary with, (i) the choice of the MD approach (i.e., AIMD or FF-based) to generate the guiding nuclear trajectory; (ii) the choice of the employed DFT functional (i.e., PBE, PBE0, B3LYP) to compute NACs or, equivalently, the wave function time-overlaps; (iii) the choice of the TSH scheme to model the NA dynamics (i.e., FSSH, DISH, mSDM, or IDA); and (iv) the size and the hydration degree (none to full coverage) of titania nanoclusters.

First, we analyze the role of the MD approach as well as the effect of the density functional choice for computing excitation energies and NACs (Figure 6). When the PBE functional is used to compute NACs, the FFMD trajectory yields faster recombination compared to using the AIMD trajectory (see blue vs red lines in Figure 6e,g), except for $(TiO_2)_4$ (blue vs red lines, Figure 6a). This trend is reversed when the hybrid B3LYP functional is used to compute NACs (green vs black lines, Figure 6a,e,g). These differences are more pronounced when computed population relaxation is fast such as in when the FSSH method is used (Figure 6a,c,e,g). The differences diminish when decoherence corrections are included and the dynamics is slower, such when the mSDM method is used (Figure 6 panels b, d, f, h). The fast FSSH-based dynamics is controlled by the coherent evolution of electronic states and is strongly affected by the NAC values, which are very sensitive to the details of nuclear motion. Hence, different methods of MD trajectory generation may yield noticeable differences, although the direction of these differences depends on the particularities of the functional used to compute NACs. On the contrary, when methods that account for decoherence, such the mSDM, are used the dynamics is controlled strongly by the fluctuations of the energy gap. Such fluctuations are less sensitive to details of nuclear dynamics, resulting in the observed smaller sensitivity of the population dynamics to the nuclear trajectories. Finally, the difference in population dynamics computed along differently generated guiding trajectories diminishes in more hydrated clusters, which can

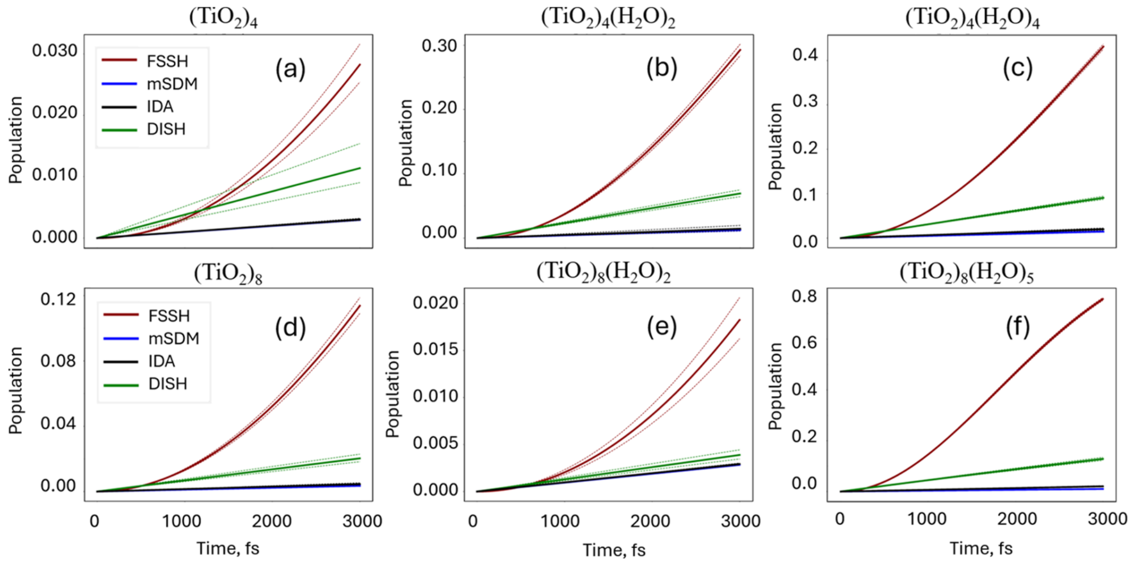

Figure 7. Evolution of the ground state S_0 population for classical FFMD and AIMD nuclear trajectories and fixed PBE functional as the underlying functional for computing the TD-DFT excitations. (a–c) and (d–f) panels illustrate $(TiO_2)_4$ and $(TiO_2)_8$ cluster in their anhydrous and hydrated counterparts. Red, blue, green, and black colored lines represent FSSH, mSDM, DISH and IDA TSH schemes, respectively. The average population for each case is shown in bold lines, whereas dashed lines account for the error bars at each NA-MD time step.

Table 1. Ground State (S_0) Recovery Times, ps, for the Six Cluster Systems Computed with Various Combinations of Guiding Trajectory Generation Method (FFMD—Top of Each Cell or AIMD—Bottom of Each Cell), NAC-Calcuations Method (TDDFT with PBE, PBE0, or B3LYP Functionals), and TSH Algorithms (FSSH, mSDM, IDA, or DISH)

method\system	$(TiO_2)_4$	$(TiO_2)_4(H_2O)_2$	$(TiO_2)_4(H_2O)_4$	$(TiO_2)_8$	$(TiO_2)_8(H_2O)_2$	$(TiO_2)_8(H_2O)_5$
PBE/FSSH	17.7 ± 1.0	5.1 ± 0.1	4.0 ± 0.0	8.6 ± 2.0	22.1 ± 1.3	2.5 ± 0.0
	15.3 ± 0.7	4.9 ± 0.1	4.2 ± 0.1	14.1 ± 0.5	8.3 ± 0.2	4.6 ± 0.1
PBE/mSDM	1013.2 ± 31.7	238.9 ± 36.7	204.1 ± 19.5	859.5 ± 85.0	1055.3 ± 16.8	294.2 ± 52.6
	981.6 ± 42.8	532.8 ± 96.0	327.0 ± 70.0	1018.0 ± 37.0	974.4 ± 60.7	469.26 ± 63.6
PBE/IDA	987.2 ± 57.6	205.5 ± 54.0	149.5 ± 18.6	657.0 ± 95.6	1024.1 ± 35.5	145.7 ± 18.6
	871.6 ± 93.1	338.4 ± 73.3	202.3 ± 53.0	923.5 ± 82.3	31.4 ± 82.4	203.7 ± 31.3
PBE/DISH	261.9 ± 68.6	41.8 ± 3.3	31.6 ± 1.3	146.0 ± 16.5	769.4 ± 94.7	21.8 ± 1.1
	67.7 ± 5.0	37.0 ± 1.5	27.6 ± 1.2	588.9 ± 104.0	194.0 ± 51.0	40.5 ± 18.0
PBE0/FSSH	11.8 ± 0.3	3.2 ± 0.0	3.4 ± 0.0	7.5 ± 0.2	18.2 ± 1.1	2.6 ± 0.1
	6.8 ± 0.1	4.9 ± 0.1	3.4 ± 0.0	8.0 ± 0.2	7.5 ± 0.2	4.4 ± 0.1
PBE0/mSDM	1014.6 ± 44.9	241.8 ± 47.2	166.7 ± 21.7	947.0 ± 64.1	1013.7 ± 49.9	128.3 ± 14.2
	511.8 ± 100.7	305.9 ± 58.6	220.3 ± 25.2	969.0 ± 52.4	718.3 ± 109.3	165.3 ± 36.7
PBE0/IDA	959.5 ± 47.7	140.7 ± 17.9	122.1 ± 23.7	907.0 ± 83.7	974.5 ± 55.0	82.5 ± 10.4
	283.6 ± 54.3	162.4 ± 21.6	107.1 ± 8.4	495.6 ± 76.6	440.6 ± 98.5	97.5 ± 11.0
PBE0/DISH	205.1 ± 27.1	57.2 ± 3.4	65.4 ± 5.6	179.2 ± 31.0	871.6 ± 79.6	45.6 ± 3.1
	104.00 ± 10.69	86.12 ± 8.67	54.6 ± 4.1	165.4 ± 19.2	112.2 ± 11.5	63.9 ± 6.4
B3LYP/FSSH	18.7 ± 1.2	4.6 ± 0.1	4.2 ± 0.1	25.1 ± 1.7	15.5 ± 1.0	2.9 ± 0.0
	8.2 ± 0.2	4.7 ± 0.1	2.5 ± 0.0	11.9 ± 0.4	9.3 ± 0.3	1.7 ± 0.0
B3LYP/mSDM	1039.04 ± 14.4	175.5 ± 28.0	179.0 ± 22.7	1024.9 ± 31.1	1033.5 ± 31.4	103.1 ± 11.1
	717.8 ± 94.0	313.3 ± 77.0	242.4 ± 35.4	929.3 ± 73.2	801.5 ± 99.9	135.0 ± 20.7
B3LYP/IDA	1004.7 ± 48.7	129.4 ± 15.9	112.8 ± 7.9	1032.7 ± 31.0	986.5 ± 43.7	67.2 ± 5.5
	416.5 ± 81.9	174.2 ± 28.0	129.0 ± 11.8	27.8 ± 73.2	587.7 ± 95.1	85.5 ± 9.3
B3LYP/DISH	246.6 ± 52.8	45.9 ± 4.2	58.3 ± 3.2	700.4 ± 83.3	686.5 ± 93.3	23.0 ± 1.3
	98.0 ± 7.6	123.3 ± 12.3	50.0 ± 3.2	212.0 ± 39.9	157.1 ± 18.3	28.7 ± 1.2

be attributed to the smaller differences in NACs and excitation energy values, as shown in Figure 4.

Second, the recombination rates computed using hybrid density functionals are generally increased compared to those computed using the semilocal PBE functional (see Figure 6 and Table 1). A plausible reason for this effect resides in the distribution of NAC values (Figure 5). The smaller NAC values are more frequently sampled when computed using the PBE functional. On the contrary, it is more probable to encounter larger NACs in the dynamics when NACs are computed using hybrid functionals. Thus, the time scales computed with hybrid functionals are generally smaller than the PBE-based counterparts, which are overestimated, $\tau_{PBE} > \tau_{PBE0} \approx \tau_{B3LYP}$. This order of the time scales is observed, with a few exceptions, for all TSH methodologies (Table 1). We stress once again that this effect stems from the multi-configurational nature of TD-DFT states, where hybrid functionals favor higher configurational mixing and increased

Table 2. Transition Dipole Moment (×10^2) between S_0 and S_1 for All Titania Systems as Computed with Different Approaches. Units are Expressed in 0.01 a.u

method\system	$(TiO_2)_4$	$(TiO_2)_4(H_2O)_2$	$(TiO_2)_4(H_2O)_4$	$(TiO_2)_8$	$(TiO_2)_8(H_2O)_2$	$(TiO_2)_8(H_2O)_5$
AIMD/TD-PBE	5.28 ± 2.97	8.32 ± 2.92	12.61 ± 5.71	9.44 ± 3.55	12.32 ± 0.20	8.81 ± 3.97
AIMD/TD-PBE0	2.82 ± 1.29	6.68 ± 2.24	7.75 ± 3.73	9.32 ± 2.42	6.59 ± 1.87	7.64 ± 2.72
AIMD/TD-B3LYP	4.21 ± 1.84	9.07 ± 3.03	9.35 ± 3.87	11.20 ± 3.67	8.51 ± 2.32	8.22 ± 2.96
FFMD/TD-PBE	6.63 ± 3.60	5.52 ± 2.70	8.00 ± 3.75	13.21 ± 6.67	9.10 ± 3.28	9.66 ± 3.65
FFMD/TD-PBE0	2.91 ± 1.24	4.68 ± 2.10	5.67 ± 2.76	6.66 ± 2.60	5.35 ± 1.83	6.70 ± 2.72
FFMD/TD-B3LYP	4.10 ± 1.30	7.45 ± 2.92	6.11 ± 2.97	7.67 ± 2.85	5.37 ± 1.97	7.81 ± 2.91

Table 3. Computed Radiative Recombination Lifetimes for All Systems; Units are expreesed in μs[a]

method\system	$(TiO_2)_4$	$(TiO_2)_4(H_2O)_2$	$(TiO_2)_4(H_2O)_4$	$(TiO_2)_8$	$(TiO_2)_8(H_2O)_2$	$(TiO_2)_8(H_2O)_5$
AIMD/TD-PBE	19.85	2.96	1.32	7.63	2.98	3.31
AIMD/TD-PBE0	22.77	2.05	1.50	2.08	3.31	1.75
AIMD/TD-B3LYP	12.91	1.31	1.25	1.87	2.50	1.85
FFMD/TD-PBE	41.28	7.01	2.81	23.95	18.82	3.16
FFMD/TD-PBE0	40.69	4.84	2.68	11.25	10.40	2.53
FFMD/TD-B3LYP	29.70	2.22	2.71	18.54	14.22	2.32

[a] The calculations are conducted for trajectories obtained via FFMD or AIMD and with different excited state calculation methods (TD-DFT with PBE, PBE0, or B3LYP functionals).

NAC magnitudes. This effect is contrary to the NAC decrease between molecular orbitals in the single-particle picture reported ealier.[93]

Third, we discuss the dependence of the recombination time scales on the TSH approaches. In general, the following order of the time scales is observed for nearly all titania systems, density functionals, and MD trajectories: $\tau_{mSDM} \geq \tau_{IDA} > \tau_{DISH(rev\ 2023)} > \tau_{FSSH}$ (see Table 1). This order is consistent with the previous assessments.[47,48,103,121,122] Among these approaches, the mSDM is perhaps the most conceptually sound and is sensitive to the details of energy gap evolution.[85] The decoherence correction generally inhibits the recombination comparing to the overcoherent FSSH description. For instance, for the $(TiO_2)_4$ system, the FSSH values vary in the 5−20 ps interval depending on the electronic structure and trajectory generation methodologies used, while the mSDM values vary in the 900−1100 ps interval. The IDA time scales are often comparable to, but usually smaller than, the mSDM values. Note that, for the same $(TiO_2)_4$ system, the IDA values vary in the 200−1000 ps interval. The former method introduces strong decoherence correction via the wave function collapse on the currently active state. Since the collapse is controlled by the hop feasibility criterion, the IDA decoherence correction is weak when the process is fast and, thus, the decoherence is consistent with the state transitions. In such situations, the IDA time scales may be comparable to the FSSH counterparts. The 2023 revision of the DISH algorithm introduces decoherence in a gradual way resembling that of the mSDM. In this approach, the superposition is either projected onto the decohered (pointer) state or such state is projected out of the coherent superposition. The surface hops are determined as in the regular FSSH. Since the stochastic wave function "diffusion" only partially affects the quantum populations of all states, the DISH_rev2023 results are often close to the FSSH, although such time scales may also be notably slower than in FSSH.

Finally, we observe a relatively faster recombination dynamics when increasing the hydration degree on the surface of titania nanoclusters (see Table 1 and Figure 7). This observation holds for nearly all nanoclusters, density functionals and TSH methodologies. Such an acceleration correlates with the trends in average NAC values (see Figure 4c,d). Indeed, Figure 4 shows that the average NAC values increase with the hydration degree as discussed earlier. Analogously, the carrier lifetimes gradually decrease as the amount of incorporated water increases (Figure 7 and Table 1). The most notable deviation from this monotonic dependence is observed for the $(TiO_2)_8(H_2O)_2$ system with the FF-based trajectory (Figure 7e and Table 1), which shows a notably slower recovery dynamics compared to the systems with lower and higher water saturation. This could be associated with the low water coverage (~25%), which is closer to the anhydrous $(TiO_2)_8$ cluster. Indeed, both systems show similar lifetimes (see Table 1). Importantly, this analysis suggests that weakly hydrated systems could be preferred for water splitting purposes, as they promote longer electron−hole recombination times which tends to enhance thephotocatalytic efficiency.

The nonradiative recombination rates computed using DISH are consistent with the previously reported values for larger $(TiO_2)_{35}$ clusters using the same TSH algorithm.[41,42] Previous time-resolved photoelectron spectroscopy (TRPES) measurements on single-crystal surfaces of anatase and rutile TiO_2 estimate the recombination times to be on the order of nanosecond,[123] which is in line with the slower recombination rates we obtain for anhydrous clusters (when accounting for electronic decoherence with the IDA or mSDM schemes). Recently the pump−probe spectroscopy experiments on bare and stoichiometric $(TiO_2)_n$ (n = 4, and 8) nanoclusters have been reported by Sayres and coauthors. The proposed rationalization of the reported measurements suggested than S_1 decay times to be on the sub-picosecond order.[37] Such interpretation disagrees with our current estimates of the nonradiative recombination time scales being off by orders of magnitude. While acknowledging the value of the experimental data, our current calculations suggest an alternative interpretation of these measurements. It is possible that these remarkably fast decay times may be indicative of an ultrafast relaxation from higher excited states to optically forbidden (dark) levels, rather than representing the carrier recombination process between the first excited and the ground state. This could be in agreement with the different order of magnitude in the lifetimes: excited state relaxation in the experimental work (with sub-ps time scales) versus lowest excited state decay studied in this work (with sub-ns time scales).

3.4. Radiative Recombination. While the previous section has extensively analyzed nonradiative recombination processes, which, due to their influence on charge carrier dynamics and efficiency, are often dominant in titania nanoparticles, it is instructional to consider the contribution of radiative recombination, which is crucial for applications where photoluminescence, light emission, or optical properties are the key performance indicators. Our calculations of the transition dipole moments (TDM) and corresponding radiative lifetimes are summarized in Tables 2 and 3, respectively. Expectedly, the computed radiative lifetimes are orders of magnitude larger compared to the nonradiative recombination ones and reach microsecond (μs) scales. Thus, the deactivation of excited states in bare and hydrated titania nanoclusters is dominated by the nonradiative recombination mechanisms.

Although we consider only a limited number of systems, we do observe several notable trends. First, for the bare nanoclusters, the radiative recombination is faster in the larger $(TiO_2)_8$ nanocluster than in the smaller one, $(TiO_2)_4$ (Table 3). This effect can be attributed to a sizable difference of the TDMs, which are larger in $(TiO_2)_8$ than in $(TiO_2)_4$ by a factor of 2−3 (Table 2), leading to the expected 4−9-fold acceleration due to the quadratic dependence of radiative recombination time scales on the TDM magnitude. The larger TDMs in the larger nanoclusters can be attributed to a greater capability for holes and electrons to separate spatially in the larger nanoclusters and hence create a larger dipole. While the actual ratio $\tau_{(TiO_2)_8}/\tau_{(TiO_2)_4}$ varies from 3 to 11 for the calculations involving DFT-based guiding trajectories, in agreement with the expectation, it is smaller for the FF-based guiding trajectories and varies between 2 and 4. This discrepancy can be attributed to the respective energy gap differences (entering the time scales formula, eq 2 cubically). While for the DFT-based trajectories, the difference of energy gaps for the two systems is negligible, the gaps obtained from the FF-based trajectories vary more notably across the two systems. This effect slows down the recombination in larger nanoclusters to a greater extent than in the smallest one, acting in the opposite way to the TDM and hence reducing the differences caused by the TDM differences. However, this effect is still dominated by the large difference in TDMs, leading to the overall acceleration of the radiative recombination in larger nanoclusters.

The second trend we observe is a gradual acceleration of the radiative recombination in the hydrated nanoclusters. As observed from Table 3, the acceleration generally correlates with the degree of hydration, although this trend may be violated for even larger hydrated nanoclusters not considered in this work. The general acceleration of the radiative recombination can be attributed mainly to the increase of the energy gap. This increase is nearly monotonic for progressively hydrated $(TiO_2)_4$ and $(TiO_2)_8$ systems. In addition, for $(TiO_2)_4$ systems, the TDM systematically increases with the degree of hydration, leading to a clear trend in computed radiative recombination time scales. For hydrated $(TiO_2)_8$ systems, there is no clear trend in the TDM as a function of hydration degree. Thus, the dependence of the radiative recombination time scales on the hydration degree is less pronounced for these systems—a notable decrease of the recombination time is observed only while moving from $(TiO_2)_8(H_2O)_2$ to $(TiO_2)_8(H_2O)_5$.

Another set of notable observations concerns the dependence of the computed recombination time scales on the combination of methods used. First, the use of the FFs for generating guiding nuclear trajectories leads to the 2−3-fold larger radiative recombination time scales compared to those obtained from the DFT-based AIMD guiding trajectories. As follows from Figure 4a,b, the FF-based trajectories show notably smaller energy gaps compared to the AIMD counterpart, although this difference decreases with the increased surface hydration degree. Consequently, smaller energy gaps lead to slower radiative recombination and hence larger radiative recombination times. As the difference of the excitation energies predicted by different methods decreases for more hydrated clusters, the radiative lifetimes become more robust with respect to the choice of the guiding trajectory generation approach. Finally, the use of PBE, PBE0, or B3LYP functionals does not greatly affect the results as far as the computations of radiative recombination times is concerned.

As presented in the previous section, nonradiative recombination processes in titania nanoclusters occur on a time scale of nanoseconds, significantly affecting the charge carrier dynamics by quickly removing the electron−hole pairs. In contrast, our analysis of radiative recombination shows that these processes occur at much slower rates, typically on the order of microseconds. The dominance of nonradiative recombination suggests that the majority of excited states decay through these nonradiative mechanisms, leaving only a small fraction of electron−hole pairs available for photon emission. Consequently, the observed photoluminescence and other radiative outputs are relatively weak, which aligns with prior studies.[124]

4. CONCLUSIONS

In this work, we present a comprehensive computational characterization of the radiative and nonradiative recombination dynamics in a series of small bare and hydrated titania nanoclusters: $(TiO_2)_n(H_2O)_m$ for $n = 4$ and 8. We find that increasing the degree of hydration tends to accelerate both radiative and nonradiative relaxation processes. The acceleration of nonradiative relaxation is attributed to the stronger influence of hydroxyl group vibrations, which significantly perturb the electronic states. In this way, the increasing delocalization and isotropy of the charge distribution in increasingly hydrated nanoclusters facilitate orbital degeneracies, enhancing nonadiabatic couplings and thus nonradiative recombination rates. The nonadiabatic couplings are found to linearly increase with the degree of hydration in the smaller $(TiO_2)_4(H_2O)_m$ nanoclusters and linearly increase after an initial plateau in the larger $(TiO_2)_8(H_2O)_m$ nanoclusters. This also indicates the diminishing influence of hydration in larger systems. Faster radiative recombination in more highly hydrated systems is rationalized by the increased excitation energy of such systems. Interestingly, our calculations predict faster radiative recombination in the bare $(TiO_2)_8$ cluster compared to its smaller counterpart, $(TiO_2)_4$. We attribute this difference to the larger electron−hole separation in the bare

$(TiO_2)_8$ cluster, which creates a larger transition dipole moment, hence stimulating the radiative recombination.

We find that the nonradiative $S_1 \rightarrow S_0$ transition is driven primarily by the vibrational modes in the 500−1000 cm^{-1} range which typically correspond to Ti−O−Ti angle bending and related modes. Based on the results of our nonradiative recombination calculation in the studied titania nanoclusters, we suggest that the time scales reported in the recent experimental work on similar-sized TiO_2 nanoclusters by Garcia et al.[37] is more likely to be attributed to the relaxation of higher excited states rather than to the electron−hole recombination process.

Finally, this work reports a detailed comparative analysis of various methodological choices possible for such dynamical calculations. We find that, for all studied systems, the dependence of the computed nonradiative and radiative time scales on the choice of the density functional used in the TD-DFT/NA-MD calculations is relatively weak. On the other hand, the nonradiative time scales are strongly dependent on the choice of the TSH approach: they are normally orders of magnitude larger when decoherence-corrected methods such as mSDM, IDA, or DISH are used compared to those obtained with methods lacking such correction, such as FSSH. The time scales obtained with decoherence-corrected methods are in good agreement with previous findings for similar systems. We also find a notable dependence of both radiative and nonradiative time scales on the method used to obtain the guiding MD trajectory. The presently employed titania FFs favor more symmetrical structures and vibrational modes compared to those in the DFT-based AIMD trajectories. As a result, the excitation energies for titania nanocluster trajectories obtained with these FFs are systematically underestimated with respect to those derived from AIMD trajectories, leading both to faster nonradiative recombination and to slower radiative recombination, especially in bare titania clusters. The reported differences are less pronounced in the hydrated systems, where both approaches lead to more consistent time scales. We argue that the limitations of the FFs can be addressed with improved parametrizations, in which case FFs may become a computationally efficient alternative to direct AIMD simulations, especially for larger nanoclusters.

■ ASSOCIATED CONTENT

Data Availability Statement

Detailed scripts and input files used for all types of calculations are available in digital form online at Zenodo server.[125]

Supporting Information

The Supporting Information is available free of charge at https://pubs.acs.org/doi/10.1021/acs.jpcc.4c07180.

> Details on the power and influence spectra for $(TiO_2)_4$, TD-PBE0, and TD-B3LYP MO isosurfaces, squares of the largest CI coefficient for S_1, total dipole moments of S_0/S_1 states, first excited state energies, nonadiabatic couplings between S_0 and S_1, and S_0 population evolution for all clusters and methodologies (PDF)

■ AUTHOR INFORMATION

Corresponding Authors

Ángel Morales-García − *Departament de Ciència de Materials i Química Física & Institut de Química Teòrica i Computacional (IQTCUB), Universitat de Barcelona, 08028 Barcelona, Spain*; orcid.org/0000-0003-0491-1234; Email: angel.morales@ub.edu

Alexey V. Akimov − *Department of Chemistry, University at Buffalo, The State University of New York, Buffalo, New York 14260, United States*; orcid.org/0000-0002-7815-3731; Email: alexeyak@buffalo.edu; @AkimovLab

Stefan T. Bromley − *Departament de Ciència de Materials i Química Física & Institut de Química Teòrica i Computacional (IQTCUB), Universitat de Barcelona, 08028 Barcelona, Spain; Institució Catalana de Recerca i Estudis Avançats (ICREA), 08010 Barcelona, Spain*; orcid.org/0000-0002-7037-0475; Email: s.bromley@ub.edu

Authors

Miguel Recio-Poo − *Departament de Ciència de Materials i Química Física & Institut de Química Teòrica i Computacional (IQTCUB), Universitat de Barcelona, 08028 Barcelona, Spain*

Mohammad Shakiba − *Department of Chemistry, University at Buffalo, The State University of New York, Buffalo, New York 14260, United States*; orcid.org/0000-0002-4110-7627

Francesc Illas − *Departament de Ciència de Materials i Química Física & Institut de Química Teòrica i Computacional (IQTCUB), Universitat de Barcelona, 08028 Barcelona, Spain*; orcid.org/0000-0003-2104-6123

Complete contact information is available at: https://pubs.acs.org/10.1021/acs.jpcc.4c07180

Notes

The authors declare no competing financial interest.

■ ACKNOWLEDGMENTS

M.R.-P., F.I., S.T.B., and Á.M.-G. thank the financial support from MCIN/AEI/10.13039/501100011033 through projects PID2020-115293RJ-I00, PID2021-126076NB-I00, PID2021-127957NB-100, TED2021-129506B-C22, TED2021-132550B-C22, and the *María de Maeztu* CEX2021-001202-M project and from the *Generalitat de Catalunya* through the projects 2021-SGR-00079 and 2021-SGR-00354. *Red de investigación* RED2022-134295-T (FOTOFUEL) is also partly acknowledged. The reported research is also involved in the European Cooperation in Science and Technology (COST) Actions: CA18234 (CompNanoEnergy) and CA21101 (COSY). M.R.-P. acknowledges the *Ministerio de Ciencia e Innovación* (MICIN) for a *Formación Personal Investigador* (FPI) fellowship (PRE2019-087627). M.R.-P., F.I., S.T.B., and A.M.G. also thank the *Red Española de Supercomputación* (RES) for the provision of supercomputing time. M.S. and A.V.A. acknowledge the financial support of the National Science Foundation (Grant NSF-2045204). Computational support is provided by the Center for Computational Research at the University at Buffalo.

■ REFERENCES

(1) Lewis, N. S. Research opportunities to advance solar energy utilization. *Science* **2016**, *351* (6271), No. aad1920.

(2) Hota, P.; Das, A.; Maiti, D. K. A short review on generation of green fuel hydrogen through water splitting. *Int. J. Hydrogen Energy* **2023**, *48* (2), 523−541.

(3) Tan, H. L.; Abdi, F. F.; Ng, Y. H. Heterogeneous photocatalysts: an overview of classic and modern approaches for optical, electronic,

and charge dynamics evaluation. *Chem. Soc. Rev.* **2019**, *48* (5), 1255−1271.

(4) Balapure, A.; Dutta, J. R.; Ganesan, R. Recent advances in semiconductor heterojunctions: a detailed review of the fundamentals of photocatalysis, charge transfer mechanism and materials. *RSC Appl. Interfaces* **2024**, *1* (1), 43−69.

(5) Wang, H.; Li, X.; Zhao, X.; Li, C.; Song, X.; Zhang, P.; Huo, P.; Li, X. A review on heterogeneous photocatalysis for environmental remediation: From semiconductors to modification strategies. *Chin. J. Catal.* **2022**, *43* (2), 178−214.

(6) Nijamudheen, A.; Akimov, A. V. Quantum Dynamics Effects in Photocatalysis. In *Visible-Light-Active Photocatalysis: Nanostructured Catalyst Design, Mechanisms, and Applications*; Ghosh, S., Ed.; Wiley-VCH Verlag Gmbh & Co. KGaA: Weinheim, 2018; pp 527−566.

(7) Djurišić, A. B.; He, Y.; Ng, A. Visible-light photocatalysts: Prospects and challenges. *APL Mater.* **2020**, *8* (3), No. 030903.

(8) Ibhadon, A. O.; Fitzpatrick, P. Heterogeneous photocatalysis: recent advances and applications. *Catalysts* **2013**, *3*, 189−218.

(9) Schneider, J.; Matsuoka, M.; Takeuchi, M.; Zhang, J.; Horiuchi, Y.; Anpo, M.; Bahnemann, D. W. Understanding TiO_2 photocatalysis: mechanisms and materials. *Chem. Rev.* **2014**, *114*, 9919−9986.

(10) Kumaravel, V.; Mathew, S.; Bartlett, J.; Pillai, S. C. Photocatalytic hydrogen production using metal doped TiO_2: A review of recent advances. *Appl. Catal., B* **2019**, *244*, 1021−1064.

(11) Ardo, S.; Meyer, G. J. Photodriven heterogeneous charge transfer with transition-metal compounds anchored to TiO_2 semiconductor surfaces. *Chem. Soc. Rev.* **2009**, *38*, 115−164.

(12) Bai, Y.; Mora-Seró, I.; De Angelis, F.; Bisquert, J.; Wang, P. Titanium dioxide nanomaterials for photovoltaic applications. *Chem. Rev.* **2014**, *114*, 10095−10130.

(13) Valero, R.; Morales-Garcia, A.; Illas, F. Theoretical modeling of electronic excitations of gas-phase and solvated TiO_2 nanoclusters and nanoparticles of interest in photocatalysis. *J. Chem. Theory Comput.* **2018**, *14*, 4391−4404.

(14) Akimov, A. V.; Neukirch, A. J.; Prezhdo, O. V. Theoretical insights into photoinduced charge transfer and catalysis at metal oxide surfaces. *Chem. Rev.* **2013**, *113*, 4496.

(15) Dahl, M.; Liu, Y.; Yin, Y. Composite titanium dioxide nanomaterials. *Chem. Rev.* **2014**, *114* (19), 9853−9889.

(16) Pagliaro, M.; Palmisano, G.; Ciriminna, R.; Loddo, V. Nanochemistry aspects of titania in dye-sensitized solar cells. *Energy Environ. Sci.* **2009**, *2*, 838−844.

(17) Adachi, M.; Murata, Y.; Takao, J.; Jiu, J.; Sakamoto, M.; Wang, F. Highly efficient dye-sensitized solar cells with a titania thin-film electrode composed of a network structure of single-crystal-like TiO_2 nanowires made by the "oriented attachment" mechanism. *J. Am. Chem. Soc.* **2004**, *126*, 14943−14949.

(18) Prasad, R. M. B.; Pathan, H. M. Effect of photoanode surface coverage by a sensitizer on the photovoltaic performance of titania based CdS quantum dot sensitized solar cells. *Nanotechnology* **2016**, *27*, No. 145402.

(19) Akhter, P.; Arshad, A.; Saleem, A. M.; Hussain, M. Recent development in non-metal-doped titanium dioxide photocatalysts for different dyes degradation and the study of their strategic factors: A review. *Catalysts* **2022**, *12*, 1331.

(20) Wang, X.; Sun, M.; Murugananthan, M.; Zhang, Y.; Zhang, L. Electrochemically self-doped WO_3/TiO_2 nanotubes for photocatalytic degradation of volatile organic compounds. *Appl. Catal., B* **2020**, *260*, No. 118205.

(21) Hassan, S. M.; Ahmed, A. I.; Mannaa, M. A. Preparation and characterization of SnO_2 doped TiO_2 nanoparticles: Effect of phase changes on the photocatalytic and catalytic activity. *J. Sci.: Adv. Mater. Devices* **2019**, *4*, 400−412.

(22) Fu, Y. S.; Li, J.; Li, J. Metal/semiconductor nanocomposites for photocatalysis: fundamentals, structures, applications and properties. *Nanomaterials* **2019**, *9*, 359.

(23) Yang, H. G.; Sun, C. H.; Qiao, S. Z.; Zou, J.; Liu, G.; Smith, S. C.; Cheng, H. M.; Lu, G. Q. Anatase TiO2 single crystals with a large percentage of reactive facets. *Nature* **2008**, *453*, 638−641.

(24) Liu, G.; Jimmy, C. Y.; Lu, G. Q. M.; Cheng, H. M. Crystal facet engineering of semiconductor photocatalysts: motivations, advances, and unique properties. *Chem. Commun.* **2011**, *47*, 6763−6783.

(25) Wang, S.; Liu, G.; Wang, L. Crystal facet engineering of photoelectrodes for photoelectrochemical water splitting. *Chem. Rev.* **2019**, *119*, 5192−5247.

(26) Morales-García, Á.; Escatllar, A. M.; Illas, F.; Bromley, S. T. Understanding the interplay between size, morphology and energy gap in photoactive TiO_2 nanoparticles. *Nanoscale* **2019**, *11*, 9032−9041.

(27) Mino, L.; Morales-García, Á.; Bromley, S. T.; Illas, F. Understanding the nature and location of hydroxyl groups on hydrated titania nanoparticles. *Nanoscale* **2021**, *13*, 6577−6585.

(28) Recio-Poo, M.; Morales-García, Á.; Illas, F.; Bromley, S. T. Crystal properties without crystallinity? Influence of surface hydroxylation on the structure and properties of small TiO2 nanoparticles. *Nanoscale* **2023**, *15*, 4809−4820.

(29) García-Romeral, N.; Keyhanian, M.; Morales-Garcia, A.; Viñes, F.; Illas Riera, F. Understanding the Chemical Bond in Semiconductor/MXene Composites: TiO_2 Clusters Anchored on the Ti_2C MXene Surface. *Chem. − Eur. J.* **2024**, *30*, No. e202400255.

(30) Alls, M.; Remesal, E. R.; Illas, F.; Morales-García, Á. Structural and Electronic Properties of Metal/Oxide Nanostructures from First-Principles: Ru_{13} Supported on $(TiO_2)_{84}$ as a Case Study. *Adv. Theory Simul.* **2023**, *6*, No. 2200670.

(31) Remesal, E. R.; Morales-García, Á. Carbon-doped anatase titania nanoparticles: similarities and differences with respect to bulk and extended surface models. *Phys. Chem. Chem. Phys.* **2022**, *24*, 21381−21387.

(32) Remesal, E. R.; Morales-García, Á.; Illas, F. Role of N Doping in the Reduction of Titania Nanostructures. *J. Phys. Chem. C* **2023**, *127*, 20128−20136.

(33) Morales-García, Á.; Viñes, F.; Sousa, C.; Illas, F. Toward a Rigorous Theoretical Description of Photocatalysis Using Realistic Models. *J. Phys. Chem. Lett.* **2023**, *14*, 3712−3720.

(34) Bao, J.; Yu, Z.; Gundlach, L.; Benedict, J. B.; Coppens, P.; et al. Excitons and excess electrons in nanometer size molecular polyoxotitanate clusters: electronic spectra, exciton dynamics, and surface states. *J. Phys. Chem. B* **2013**, *117*, 4422−4430.

(35) Bao, J.; Gundlach, L.; Yu, Z.; Benedict, J. B.; Snoeberger, R. C., III; et al. Hot hole hopping in a polyoxotitanate cluster terminated with catechol electron donors. *J. Phys. Chem. C* **2016**, *120*, 20006−20015.

(36) Obara, Y.; Ito, H.; Ito, T.; Kurahashi, N.; Thürmer, S.; et al. Femtosecond time-resolved X-ray absorption spectroscopy of anatase TiO_2 nanoparticles using XFEL. *Struct. Dyn.* **2017**, *4*, No. 044033.

(37) Garcia, J. M.; Heald, L. F.; Shaffer, R. E.; Sayres, S. G. Oscillation in Excited State Lifetimes with Size of Sub-nanometer Neutral $(TiO_2)_n$ Clusters Observed with Ultrafast Pump−Probe Spectroscopy. *J. Phys. Chem. Lett.* **2021**, *12*, 4098−4103.

(38) Berardo, E.; Hu, H. S.; Shevlin, S. A.; Woodley, S. M.; Kowalski, K.; Zwijnenburg, M. A. Modeling excited states in TiO_2 nanoparticles: on the accuracy of a TD-DFT based description. *J. Chem. Theory Comput.* **2014**, *10*, 1189−1199.

(39) Cho, D.; Ko, K. C.; Lamiel-Garcia, O.; Bromley, S. T.; Lee, J. Y.; Illas, F. Effect of size and structure on the ground-state and excited-state electronic structure of TiO_2 nanoparticles. *J. Chem. Theory Comput.* **2016**, *12*, 3751−3763.

(40) Valero, R.; Morales-García, Á.; Illas, F. Investigating the character of excited states in TiO_2 nanoparticles from topological descriptors: implications for photocatalysis. *Phys. Chem. Chem. Phys.* **2020**, *22*, 3017−3029.

(41) Nam, Y.; Li, L.; Lee, J. Y.; Prezhdo, O. V. Size and shape effects on charge recombination dynamics of TiO_2 nanoclusters. *J. Phys. Chem. C* **2018**, *122*, 5201−5208.

(42) Nam, Y.; Li, L.; Lee, J. Y.; Prezhdo, O. V. Strong influence of oxygen vacancy location on charge carrier losses in reduced TiO_2 nanoparticles. *J. Phys. Chem. Lett.* **2019**, *10*, 2676−2683.

(43) Sousa, C.; Tosoni, S.; Illas, F. Theoretical approaches to excited-state-related phenomena in oxide surfaces. *Chem. Rev.* **2013**, *113*, 4456−4495.

(44) Livraghi, S.; Paganini, M. C.; Giamello, E.; Selloni, A.; Di Valentin, C.; Pacchioni, G. Origin of photoactivity of nitrogen-doped titanium dioxide under visible light. *J. Am. Chem. Soc.* **2006**, *128*, 15666−15671.

(45) Migani, A.; Blancafort, L. What controls photocatalytic water oxidation on rutile TiO_2 (110) under ultra-high-vacuum conditions? *J. Am. Chem. Soc.* **2017**, *139*, 11845−11856.

(46) Jiang, X.; Zheng, Q.; Lan, Z.; Saidi, W. A.; Ren, X.; Zhao, J. Real-time GW-BSE investigations on spin-valley exciton dynamics in monolayer transition metal dichalcogenide. *Sci. Adv.* **2021**, *7*, No. eabf3759.

(47) Smith, B.; Shakiba, M.; Akimov, A. V. Nonadiabatic dynamics in Si and CdSe nanoclusters: many-body vs single-particle treatment of excited states. *J. Chem. Theory Comput.* **2021**, *17*, 678−693.

(48) Smith, B.; Shakiba, M.; Akimov, A. V. Crystal symmetry and static electron correlation greatly accelerate nonradiative dynamics in lead halide perovskites. *J. Phys. Chem. Lett.* **2021**, *12*, 2444−2453.

(49) Levine, B. G.; Ko, C.; Quenneville, J.; MartÍnez, T. J. Conical intersections and double excitations in time-dependent density functional theory. *Mol. Phys.* **2006**, *104*, 1039−1051.

(50) Liu, W.; Settels, V.; Harbach, P. H.; Dreuw, A.; Fink, R. F.; Engels, B. Assessment of TD-DFT-and TD-HF-based approaches for the prediction of exciton coupling parameters, potential energy curves, and electronic characters of electronically excited aggregates. *J. Comput. Chem.* **2011**, *32*, 1971−1981.

(51) Zhu, Y.; Long, R. Density Functional Theory Half-Electron Self-Energy Correction for Fast and Accurate Nonadiabatic Molecular Dynamics. *J. Phys. Chem. Lett.* **2021**, *12*, 10886−10892.

(52) Perdew, J. P.; Burke, K.; Ernzerhof, M. Generalized gradient approximation made simple. *Phys. Rev. Lett.* **1996**, *77*, 3865.

(53) Shao, Y.; Mei, Y.; Sundholm, D.; Kaila, V. R. Benchmarking the Performance of Time-Dependent Density Functional Theory Methods on Biochromophores. *J. Chem. Theory Comput.* **2020**, *16*, 587−600.

(54) Kretz, B.; Egger, D. A. Accurate non-adiabatic couplings from optimally tuned range-separated hybrid functionals. *J. Chem. Phys.* **2022**, *157*, No. 101104.

(55) Smith, B.; Akimov, A. V. Hot Electron Cooling in Silicon Nanoclusters via Landau-Zener Nonadiabatic Molecular Dynamics: Size Dependence and Role of Surface Termination. *J. Phys. Chem. Lett.* **2020**, *11*, 1456−1465.

(56) Zhang, Z.; He, J.; Long, R. Ultrafast Charge Separation and Recombination across a Molecule/$CsPbBr_3$ Quantum Dot Interface from First-Principles Nonadiabatic Molecular Dynamics Simulation. *J. Phys. Chem. C* **2019**, *123*, 23800−23806.

(57) Fu, J.; Li, M.; Kang, Y.; Yang, K.; Li, H.; Zhang, J.; Ma, W. Water dopant control of structural stability and charge recombination of perovskite solar cells: A first-principles study. *Appl. Surf. Sci.* **2023**, *612*, No. 155794.

(58) Nelson, T.; Fernandez-Alberti, S.; Roitberg, A. E.; Tretiak, S. Nonadiabatic excited-state molecular dynamics: Modeling photophysics in organic conjugated materials. *Acc. Chem. Res.* **2014**, *47*, 1155−1164.

(59) Shakiba, M.; Stippell, E.; Li, W.; Akimov, A. V. Nonadiabatic Molecular Dynamics with Extended Density Functional Tight-Binding: Application to Nanocrystals and Periodic Solids. *J. Chem. Theory Comput.* **2022**, *18*, 5157−5180.

(60) Duncan, W. R.; Prezhdo, O. V. Theoretical studies of photoinduced electron transfer in dye sensitized TiO_2. *Annu. Rev. Phys. Chem.* **2007**, *58*, 143−184.

(61) Zhang, L.; Chu, W.; Zhao, C.; Zheng, Q.; Prezhdo, O. V.; Zhao, J. Dynamics of photoexcited small polarons in transition-metal oxides. *J. Phys. Chem. Lett.* **2021**, *12*, 2191−2198.

(62) Muuronen, M.; Parker, S. M.; Berardo, E.; Le, A.; Zwijnenburg, M. A.; Furche, F. Mechanism of photocatalytic water oxidation on small TiO_2 nanoparticles. *Chem. Sci.* **2017**, *8* (3), 2179−2183.

(63) Rotteger, C. H.; Jarman, C. K.; Sutton, S. F.; Sayres, S. G. Size onset of metallic behavior in neutral aluminum clusters. *Nanoscale* **2024**, *16* (28), 13516−13524.

(64) Rotteger, C. H.; Jarman, C. K.; Sobol, M. M.; Sutton, S. F.; Sayres, S. G. Sub-picosecond photodynamics of small neutral copper oxide clusters. *Phys. Chem. Chem. Phys.* **2024**, *26* (31), 20937−20946.

(65) Rotteger, C. H.; Jarman, C. K.; Sobol, M. M.; Sutton, S. F.; Sayres, S. G. Subpicosecond Dynamics of Rydberg Excitons Produced from Ultraviolet Excitation of Neutral Cuprite (Cu_2O) n Clusters, n < 13. *J. Phys. Chem. A* **2024**, *128* (39), 8466−8472.

(66) Cuko, A.; Escatllar, A. M.; Calatayud, M.; Bromley, S. T. Properties of hydrated TiO_2 and SiO_2 nanoclusters: dependence on size, temperature and water vapour pressure. *Nanoscale* **2018**, *10*, 21518−21532.

(67) Weichman, M. L.; Debnath, S.; Kelly, J. T.; Gewinner, S.; Schöllkopf, W.; Neumark, D. M.; Asmis, K. R. Dissociative water adsorption on gas-phase titanium dioxide cluster anions probed with infrared photodissociation spectroscopy. *Top. Catal.* **2018**, *61*, 92−105.

(68) Yin, S.; Bernstein, E. R. Experimental and theoretical studies of H 2 O oxidation by neutral Ti 2 O 4, 5 clusters under visible light irradiation. *Phys. Chem. Chem. Phys.* **2014**, *16* (27), 13900−13908.

(69) Wang, T. H.; Fang, Z.; Gist, N. W.; Li, S.; Dixon, D. A.; Gole, J. L. Computational study of the hydrolysis reactions of the ground and first excited triplet states of small TiO2 nanoclusters. *J. Phys. Chem. C* **2011**, *115* (19), 9344−9360.

(70) Kasha, M. Characterization of Electronic Transitions in Complex Molecules. *Discuss. Faraday Soc.* **1950**, *9*, 14−19.

(71) Shakiba, M.; Smith, B.; Li, W.; Dutra, M.; Jain, A.; Sun, X.; Garashchuk, S.; Akimov, A. Libra: A Modular Software Library for Quantum Nonadiabatic Dynamics. *Software Impacts* **2022**, *14*, No. 100445.

(72) Akimov, A. V. Libra: An Open-Source "Methodology Discovery" Library for Quantum and Classical Dynamics Simulations. *J. Comput. Chem.* **2016**, *37*, 1626−1649.

(73) Akimov, A. V.; Shakiba, M.; Smith, B.; Dutra, M.; Han, D.; Sato, K.; Temen, S.; Li, W.; Khvorost, T.et al. *Libra v5.7.1*, Zenodo, 2024.

(74) Kühne, T. D.; Iannuzzi, M.; Del Ben, M.; Rybkin, V. V.; Seewald, P.; et al. CP2K: An electronic structure and molecular dynamics software package-Quickstep: Efficient and accurate electronic structure calculations. *J. Chem. Phys.* **2020**, *152*, No. 194103.

(75) Lamiel-Garcia, O.; Cuko, A.; Calatayud, M.; Illas, F.; Bromley, S. T. Predicting size-dependent emergence of crystallinity in nanomaterials: titania nanoclusters versus nanocrystals. *Nanoscale* **2017**, *9*, 1049−1058.

(76) Gale, J. D. GULP: A computer program for the symmetry-adapted simulation of solids. *J. Chem. Soc., Faraday Trans.* **1997**, *93*, 629−637.

(77) Gale, J. D.; Rohl, A. L. The general utility lattice program (GULP). *Mol. Simul.* **2003**, *29*, 291−341.

(78) VandeVondele, J.; Hutter, J. Gaussian basis sets for accurate calculations on molecular systems in gas and condensed phases. *J. Chem. Phys.* **2007**, *127*, No. 114105.

(79) Hartwigsen, C.; Goedecker, S.; Hutter, J. Relativistic separable dual-space Gaussian pseudopotentials from H to Rn. *Phys. Rev. B* **1998**, *58*, 3641.

(80) Grimme, S.; Antony, J.; Ehrlich, S.; Krieg, H. A consistent and accurate ab initio parametrization of density functional dispersion correction (DFT-D) for the 94 elements H-Pu. *J. Chem. Phys.* **2010**, *132*, No. 154104.

(81) Hinuma, Y.; Hayashi, H.; Kumagai, Y.; Tanaka, I.; Oba, F. Comparison of approximations in density functional theory calculations: Energetics and structure of binary oxides. *Phys. Rev. B* **2017**, *96* (9), No. 094102.

(82) Agosta, L.; Brandt, E. G.; Lyubartsev, A. P. Diffusion and reaction pathways of water near fully hydrated TiO2 surfaces from ab

initio molecular dynamics. *J. Chem. Phys.* **2017**, *147* (2), No. 024704, DOI: 10.1063/1.4991381.

(83) Fritsch, D. Amorphous Sn-Ti Oxides: A Combined Molecular Dynamics and Density Functional Theory Study. *Phys. Status Solidi A* **2018**, *215* (13), No. 1800071.

(84) Ohto, T.; Dodia, M.; Xu, J.; Imoto, S.; Tang, F.; Zysk, F.; Kühne, T. D.; Shigeta, Y.; Bonn, M.; Wu, X.; Nagata, Y. Accessing the accuracy of density functional theory through structure and dynamics of the water−air interface. *J. Phys. Chem. Lett.* **2019**, *10* (17), 4914−4919.

(85) Evans, D. J.; Holian, B. L. The nose−hoover thermostat. *J. Chem. Phys.* **1985**, *83*, 4069−4074.

(86) Martinez, M.; Gaigeot, M. P.; Borgis, D.; Vuilleumier, R. Extracting effective normal modes from equilibrium dynamics at finite temperature. *J. Chem. Phys.* **2006**, *125*, No. 144106.

(87) Akimov, A. V.; Prezhdo, O. V. Persistent electronic coherence despite rapid loss of electron−nuclear correlation. *J. Phys. Chem. Lett.* **2013**, *4*, 3857−3864.

(88) Hilborn, R. C. Einstein coefficients, cross sections, *f* values, dipole moments, and all that. *Am. J. Phys.* **1982**, *50*, 982−986.

(89) Löwdin, P.-O. Quantum theory of many-particle systems. I. Physical interpretations by means of density matrices, natural spin-orbitals, and convergence problems in the method of configurational interaction. *Phys. Rev.* **1955**, *97*, 1474.

(90) Hammes-Schiffer, S.; Tully, J. C. Proton Transfer in Solution: Molecular Dynamics with Quantum Transitions. *J. Chem. Phys.* **1994**, *101*, 4657−4667.

(91) Adamo, C.; Barone, V. Toward reliable density functional methods without adjustable parameters: The PBE0 model. *J. Chem. Phys.* **1999**, *110*, 6158−6170.

(92) Becke, A. D. A new mixing of Hartree−Fock and local density-functional theories. *J. Chem. Phys.* **1993**, *98*, 1372−1377.

(93) Lin, Y.; Akimov, A. V. Dependence of Nonadiabatic Couplings with Kohn-Sham Orbitals on the Choice of Density Functional: Pure *vs* Hybrid. *J. Phys. Chem. A* **2016**, *120*, 9028−9041.

(94) Shakiba, M.; Akimov, A. V. Generalization of the Local Diabatization Approach for Propagating Electronic Degrees of Freedom in Nonadiabatic Dynamics. *Theor. Chem. Acc.* **2023**, *142*, No. 68.

(95) Granucci, G.; Persico, M.; Toniolo, A. Direct Semiclassical Simulation of Photochemical Processes with Semiempirical Wave Functions. *J. Chem. Phys.* **2001**, *114*, 10608−10615.

(96) Craig, C. F.; Duncan, W. R.; Prezhdo, O. V. Trajectory surface hopping in the time-dependent Kohn-Sham approach for electron-nuclear dynamics. *Phys. Rev. Lett.* **2005**, *95*, No. 163001.

(97) Duncan, W. R.; Craig, C. F.; Prezhdo, O. V. Time-domain ab initio study of charge relaxation and recombination in dye-sensitized TiO_2. *J. Am. Chem. Soc.* **2007**, *129*, 8528−8543.

(98) Prezhdo, O. V.; Duncan, W. R.; Prezhdo, V. V. Photoinduced electron dynamics at the chromophore−semiconductor interface: A time-domain ab initio perspective. *Prog. Surf. Sci.* **2009**, *84*, 30−68.

(99) Tully, J. C. Molecular dynamics with electronic transitions. *J. Chem. Phys.* **1990**, *93*, 1061−1071.

(100) Smith, B.; Akimov, A. V. A comparative analysis of surface hopping acceptance and decoherence algorithms within the neglect of back-reaction approximation. *J. Chem. Phys.* **2019**, *151*, No. 124107.

(101) Granucci, G.; Persico, M. Critical appraisal of the fewest switches algorithm for surface hopping. *J. Chem. Phys.* **2007**, *126*, No. 134114.

(102) Nelson, T.; Fernandez-Alberti, S.; Roitberg, A. E.; Tretiak, S. Nonadiabatic excited-state molecular dynamics: Treatment of electronic decoherence. *J. Chem. Phys.* **2013**, *138*, No. 224111.

(103) Shakiba, M.; Akimov, A. V. Dependence of Electron−Hole Recombination Rates on Charge Carrier Concentration: A Case Study of Nonadiabatic Molecular Dynamics in Graphitic Carbon Nitride Monolayers. *J. Phys. Chem. C* **2023**, *127*, 9083−9096.

(104) Ohsaka, T.; Izumi, F.; Fujiki, Y. Raman spectrum of anatase, TiO_2. *J. Raman Spectrosc.* **1978**, *7*, 321−324.

(105) Hashimoto, M.; Takadama, H.; Mizuno, M.; Kokubo, T. Enhancement of mechanical strength of TiO_2/high-density polyethylene composites for bone repair with silane-coupling treatment. *Mater. Res. Bull.* **2006**, *41*, 515−524.

(106) Antony, R. P.; Dasgupta, A.; Mahana, S.; Topwal, D.; Mathews, T.; Dhara, S. Resonance Raman spectroscopic study for radial vibrational modes in ultra-thin walled TiO_2 nanotubes. *J. Raman Spectrosc.* **2015**, *46*, 231−235.

(107) Tang, H.; Prasad, K.; Sanjines, R.; Schmid, P.; Levy, F. Electrical and optical properties of TiO_2 anatase thin films. *J. Appl. Phys.* **1994**, *75*, 2042−2047.

(108) Macià Escatllar, A.; Morales-García, Á.; Illas, F.; Bromley, S. T. Efficient preparation of TiO_2 nanoparticle models using interatomic potentials. *J. Chem. Phys.* **2019**, *150*, No. 214305.

(109) Alvertis, A. M.; Schröder, F. A.; Chin, A. W. Non-equilibrium relaxation of hot states in organic semiconductors: Impact of mode-selective excitation on charge transfer. *J. Chem. Phys.* **2019**, *151* (8), No. 084104, DOI: 10.1063/1.5115239.

(110) Alvertis, A. M.; Pandya, R.; Muscarella, L. A.; Sawhney, N.; Nguyen, M.; Ehrler, B.; Rao, A.; Friend, R. H.; Chin, A. W.; Monserrat, B. Impact of exciton delocalization on exciton-vibration interactions in organic semiconductors. *Phys. Rev. B* **2020**, *102* (8), No. 081122.

(111) Ghosh, P.; Alvertis, A. M.; Chowdhury, R.; Murto, P.; Gillett, A. J.; Dong, S.; Sneyd, A. J.; Cho, H.-H.; Evans, E. W.; Monserrat, B.; et al. Decoupling excitons from high-frequency vibrations in organic molecules. *Nature* **2024**, *629* (8011), 355−362.

(112) Lu, T.; Chen, F. Multiwfn: A multifunctional wavefunction analyzer. *J. Comput. Chem.* **2012**, *33*, 580−592.

(113) Recio-Poo, M.; Morales-García, Á.; Illas, F.; Bromley, S. T. Tuning electronic levels in photoactive hydroxylated titania nanosystems: combining the ligand dipole effect and quantum confinement. *Nanoscale* **2024**, *16*, 8975−8985.

(114) Yang, S.; Prendergast, D.; Neaton, J. B. Tuning semiconductor band edge energies for solar photocatalysis via surface ligand passivation. *Nano Lett.* **2012**, *12* (1), 383−388.

(115) Zhang, D.; Yang, M.; Dong, S. Hydroxylation of the rutile TiO_2 (110) surface enhancing its reducing power for photocatalysis. *J. Phys. Chem. C* **2015**, *119* (3), 1451−1456.

(116) Verdi, C.; Giustino, F. Fröhlich electron-phonon vertex from first principles. *Phys. Rev. Lett.* **2015**, *115* (17), No. 176401.

(117) Kronik, L.; Stein, T.; Refaely-Abramson, S.; Baer, R. Excitation gaps of finite-sized systems from optimally tuned range-separated hybrid functionals. *J. Chem. Theory Comput.* **2012**, *8*, 1515−1531.

(118) Alkan, F.; Aikens, C. M. TD-DFT and TD-DFTB investigation of the optical properties and electronic structure of silver nanorods and nanorod dimers. *J. Phys. Chem. C* **2018**, *122*, 23639−23650.

(119) Zhai, H. J.; Wang, L. S. Probing the Electronic Structure and Band Gap Evolution of Titanium Oxide Clusters $(TiO_2)_n$ ($n = 1-10$) Using Photoelectron Spectroscopy. *J. Am. Chem. Soc.* **2007**, *129*, 3022−3026.

(120) Hele, T. J. H.; Monserrat, B.; Alvertis, A. M. Systematic improvement of molecular excited state calculations by inclusion of nuclear quantum motion: a mode-resolved picture and the effect of molecular size. *J. Chem. Phys.* **2021**, *154* (24), No. 244109.

(121) Zhang, Q.; Shao, X.; Li, W.; Mi, W.; Pavanello, M.; Akimov, A. V. Nonadiabatic Molecular Dynamics with Subsystem Density Functional Theory: Application to Crystalline Pentacene. *J. Phys.: Condens. Matter* **2024**, *36*, No. 385901.

(122) Akimov, A. V. Excited state dynamics in monolayer black phosphorus revisited: Accounting for many-body effects. *J. Chem. Phys.* **2021**, *155*, No. 134106.

(123) Ozawa, K.; Emori, M.; Yamamoto, S.; Yukawa, R.; Yamamoto, S.; Hobara, R.; Kazushi, F.; Hiroshi, S.; Matsuda, I. Electron−hole recombination time at TiO_2 single-crystal surfaces: Influence of surface band bending. *J. Phys. Chem. Lett.* **2014**, *5*, 1953−1957.

(124) Serpone, N.; Lawless, D.; Khairutdinov, R. Size effects on the photophysical properties of colloidal anatase TiO_2 particles: size

quantization versus direct transitions in this indirect semiconductor? *J. Phys. Chem. A* **1995**, *99* (45), 16646−16654.

(125) Recio Poo, M.; Akimov, A.; Morales, A. *AkimovLab/Project_TiO$_2$_water_met-hods_assessment: Nonadiabatic dynamics in hydrated (TiO$_2$)$_n$ clusters (v1.0.0)*, Zenodo 2024.